

# SCOPE OUT MULTIBAND GRAVITATIONAL-WAVE OBSERVATIONS OF GW190521-LIKE BINARY BLACK HOLES WITH SPACE GRAVITATIONAL WAVE ANTENNA B-DECIGO

Hiroyuki Nakano<sup>1</sup>  Ryuichi Fujita<sup>2,3</sup>  Soichiro Isoyama<sup>4</sup>  Norichika Sago<sup>5,6</sup> 

<sup>1</sup> Faculty of Law, Ryukoku University, Kyoto 612-8577, Japan;  
hinakano@law.ryukoku.ac.jp

<sup>2</sup> Institute of Liberal Arts, Otemon Gakuin University, Osaka 567-8502, Japan;

<sup>3</sup> Center for Gravitational Physics, Yukawa Institute for Theoretical Physics, Kyoto University,  
Kyoto 606-8502, Japan;  
ryuichi.fujita@yukawa.kyoto-u.ac.jp

<sup>4</sup> School of Mathematics, University of Southampton, Southampton SO17 1BJ, United Kingdom;  
isoyama@yukawa.kyoto-u.ac.jp

<sup>5</sup> Department of Physics, Kyoto University, Kyoto 606-8502, Japan;

<sup>6</sup> Advanced Mathematical Institute, Osaka City University, Osaka 558-8585, Japan; sago@tap.scphys.kyoto-u.ac.jp

\* Correspondence: hinakano@law.ryukoku.ac.jp

Received: date; Accepted: date; Published: date

**Abstract:** The gravitational wave event, GW190521 is the most massive binary black hole merger observed by ground-based gravitational wave observatories LIGO/Virgo to date. While the observed gravitational-wave signal is mainly in the merger and ringdown phases, the inspiral gravitational-wave signal of GW190521-like binary will be more visible by space-based detectors in the low-frequency band. In addition, the ringdown gravitational-wave signal will be more loud with the next generation (3G) of ground-based detectors in the high-frequency band, displaying a great potential of the multiband gravitational wave observations. In this paper, we explore the scientific potential of multiband observations of GW190521-like binaries with milli-Hz gravitational wave observatory: LISA, deci-Hz observatory: B-DECIGO, and (next generation of) hecto-Hz observatories: aLIGO and ET. In the case of quasicircular evolution, the triple-band observation by LISA, B-DECIGO and ET will provide parameter estimation errors of the masses and spin amplitudes of component black holes at the level of order 1% – 10%. This would allow consistency tests of general relativity in the strong-field at an unparalleled precision, particularly with the “B-DECIGO + ET” observation. It would also enable to probe the ergoregion of the remnant Kerr BH through the measurement of quasinormal modes by ET. In the case of eccentric evolution, the multiband signal-to-noise ratio by “B-DECIGO + ET” observation would be larger than 100 for a five year observation prior to coalescence, even with high final eccentricities.

**Keywords:** Gravitational waves; Binary black holes; Quasinormal modes; General relativity

---

## 1. Introduction

Among gravitational-wave (GW) events detected by LIGO and Virgo during O1, O2 and O3a runs [1,2], a binary black hole (BBH) merger: GW190521 [3,4] is one of the most striking discoveries. GW190521 is the heaviest BBH merger ever observed, producing the remnant black hole (BH) with the mass of

$142_{-16}^{+28} M_{\odot}$ <sup>1</sup> that can be interpreted as an intermediate mass BH; the source parameters of GW190521 (and our notations) are summarized in Table 1. This measurement triggers the intense investigation of GW190521's unique source property.

**Table 1.** Summary of the source parameters of GW190521 as a quasicircular BBH merger, reported by the LIGO-Virgo collaboration [3] based on a BBH waveform model [6]. The symmetric 90% credible interval for each parameter is also quoted. Note that the parameters are written in our notation, and masses are given in the source's rest frame; multiply by  $(1+z)$  to convert to the observer frame.

Parameter	Symbol	
Primary mass [ $M_{\odot}$ ]	$m_2^r$	$85_{-14}^{+21}$
Secondary mass [ $M_{\odot}$ ]	$m_1^r$	$66_{-18}^{+17}$
Primary spin magnitude	$ \bar{\chi}_2 $	$0.69_{-0.62}^{+0.27}$
Secondary spin magnitude	$ \bar{\chi}_1 $	$0.73_{-0.64}^{+0.24}$
Total mass [ $M_{\odot}$ ]	$m_t^r (= m_1^r + m_2^r)$	$150_{-17}^{+29}$
Mass ratio	$q (= m_1^r / m_2^r \leq 1)$	$0.79_{-0.29}^{+0.19}$
Luminosity Distance [Gpc]	$D_L$	$5.3_{-2.6}^{+2.4}$
Redshift	$z$	$0.82_{-0.34}^{+0.28}$

A key element to better understand GW190521 is the precise measurement of the binary parameters (see, for example, Ref. [7] for a possibility of an intermediate mass ratio inspiral). GW190521 is, however, much heavier BBH system than previously observed GW events, and one of the difficulties here is the short duration and bandwidth of the GW signal that can be observed in the LIGO/Virgo band. In the case of the quasicircular BBH scenario (which is most favored by the LIGO/Virgo analysis [3,4]), the coalescing time and the numbers of cycle at the GW frequency  $f$  (in the observer frame) are estimated as

$$t_c \sim 1.3 (1+z)^{-5/3} \left( \frac{m_1^r}{66M_{\odot}} \right)^{-1} \left( \frac{m_2^r}{86M_{\odot}} \right)^{-1} \left( \frac{m_t^r}{150M_{\odot}} \right)^{1/3} \left( \frac{f}{10.0 \text{ Hz}} \right)^{-8/3} \text{ s}, \quad (1)$$

$$N_c \sim 1.0 \times 10^1 (1+z)^{-5/3} \left( \frac{m_1^r}{66M_{\odot}} \right)^{-1} \left( \frac{m_2^r}{85M_{\odot}} \right)^{-1} \left( \frac{m_t^r}{150M_{\odot}} \right)^{1/3} \left( \frac{f}{10.0 \text{ Hz}} \right)^{-5/3}, \quad (2)$$

indicating the lack of the GW signals from the sufficiently long inspiral phase. Because of the short duration signal dominated by the merger and ringdown phases, for example, only weak constraints are obtained for the component BH spins and their orientations [4]. Furthermore, even alternative interpretations of the observed GW signal other than massive quasicircular BBH merger in general relativity (GR) would become more relevant; several plausible scenarios are assessed in Section 6 of Ref. [4] by the LIGO-Virgo collaboration.

At the same time, the estimation in Eqs. (1) and (2) suggests a natural way to overcome the hurdle here: observe the inspiral GW signal in the low-frequency band offered by space-based GW detectors. Future GW astronomy in 2030s will utilize the LISA observatory in the milli-Hz band [8] and deci-Hz GW detectors such as B-DECIGO [9]: a prototype GW antenna of the DECIGO mission [10,11]<sup>2</sup>. Figure 1 plots the track of the strain sensitivity curve of GW190521-like non-spinning BBH system, assuming the quasicircular evolution and a simple inspiral–merger–ringdown (IMR) amplitude model given in Eq. (16).

<sup>1</sup> We set  $G = 1 = c$  with the useful conversion factor  $1M_{\odot} = 1.477 \text{ km} = 4.926 \times 10^{-6} \text{ s}$ . We also assume a ‘‘Planck’’ flat cosmology (when it is needed) with the Hubble constant  $H_0 = 67.7 \text{ km s}^{-1} \text{ Mpc}^{-1}$ , and density parameters  $\Omega_M = 0.307$  and  $\Omega_{\Lambda} = 0.694$  [5].

<sup>2</sup> Other proposed GW missions in the low-frequency band, including Taiji [12] and TianQin [13] in the milli-Hz band, and MAGIS [14] and TianGO [15] in the deci-Hz band are concisely summarized in, for example, reviews by Ni [16,17].

At the GW frequency  $f = 0.1$  Hz, for example, Eqs. (1) and (2) give the coalescing time  $t_c \sim 1.1 \times 10^5$  s and the numbers of cycles  $N_c \sim 8.1 \times 10^3$  with the dimensionless characteristic strain

$$h_c \sim 7.6 \times 10^{-22} (1+z)^{5/6} \left( \frac{\mathcal{M}^r}{65.1 M_\odot} \right)^{5/6} \left( \frac{f}{0.1 \text{ Hz}} \right)^{-1/6} \left( \frac{D_L}{5.3 \text{ Gpc}} \right)^{-1}, \quad (3)$$

where we introduce the the source's rest-frame chirp mass  $\mathcal{M}^r \equiv v^{3/5} m_t^r$  with the symmetric mass ratio  $v \equiv m_1^r m_2^r / m_t^r{}^2$ . In fact, we find in Section 3 that the sky and polarization averaged signal-to-noise ratio (SNR) (whose meaning is momentarily clarified in Section 2) accumulated 5-years before the final coalescence would be  $\sim 5.9 \times 10^1$  in the B-DECIGO band and  $\sim 2.7$  in the LISA band. These estimations show that the early-inspiral signal of GW190521-like BBHs would be sensitive in the LISA band, and it would be even loud in the deci-Hz band.

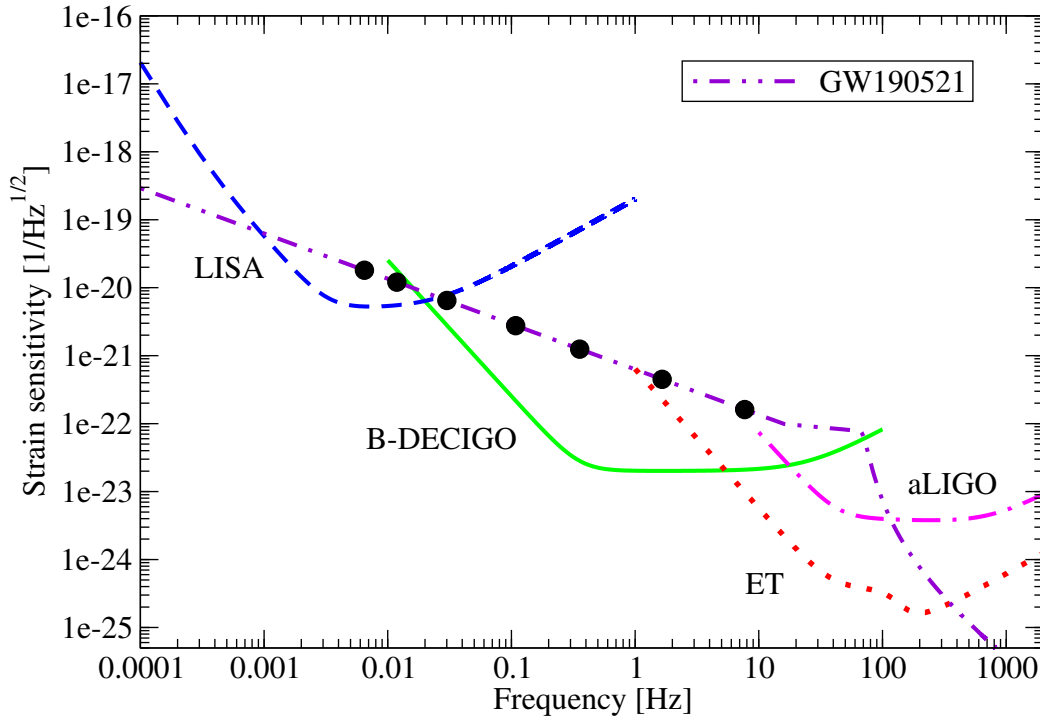


**Figure 1.** Strain sensitivity curves for ground-based aLIGO and a next-generation (3G) detector: Einstein Telescope (ET), and space-based B-DECIGO and LISA, together with the GW amplitude of GW190521-like quasicircular BBH. We use the median values in Table 1 as source parameters. The noise power spectral density (PSD) for each GW detector is given in Section 2.1, and the spectral density of BBH amplitude is obtained by the nonspinning, IMR amplitude model in Section 2.3. As a reference, we mark the black dots with 5 years, 1 year, 1 month, 1 day, 1 hour, 1 minute and 1 second before merger time (1), from the left to the right, respectively.

Although the observation with LISA and B-DECIGO alone would provide a valuable information of the inspiral GW signal from the GW190521-like BBH system, the true potential of their low-frequency sensitivity will be revealed only when it is combined with the high-frequency sensitivity in the hecto-Hz band. As illustrated in Figure 1, the late-inspiral and merger–ringdown GW signals of GW190521-like BBH are best detected with aLIGO, Virgo and KAGRA [18]. In addition to ground-based GW observatories that are online, the next generation (3G) of ground-based detectors such as Einstein Telescope (ET) [19,20] (see also Ref. [21] for Cosmic Explorer (CE)) will significantly improve the visibility of GW190521-like BBH

systems. We will see in Section 3 that the averaged SNR of the late-inspiral and ringdown signals in the ET band would be  $\sim 2.7 \times 10$  and  $\sim 1.5 \times 10^2$ , respectively. The joint “space + ground” observation across the full GW bands would be therefore the best way to observe the GW190521-like BBH systems; this is the basic idea of *multiband GW astronomy*.

Soon after the first detection of GW150914 [22], the potential of multiband GW astronomy of BBH systems with LISA and aLIGO is emphasized [23] (see also Ref. [24]). This study is immediately followed up with more detailed analyses. The works include (but not limited to) the improved estimation of source parameters [25,26], tests of GR with high precision [27–32], refined event rate estimations [33], probing environment effects [34,35], and new data analysis ideas [36]; all prove the scientific values added by the multiband observations. Among these investigations, Refs. [9,37–41] demonstrated that the multiband observation of stellar-mass BBH systems will further benefit from having (B-)DECIGO in the deci-Hz band, which naturally bridges the gap between LISA and aLIGO bands.

### 1.1. Goals and organization of this paper

Our purpose in this paper is to explore the prospects for the multiband observation of GW190521-like non-precessing, quasicircular “intermediate-mass” BBHs. The possibility of the multiband observations of intermediate-mass BBHs with deci-Hz GW detectors was pointed out by Amaro-Seoane and Santamaria [42], and Yagi [43]. We consider these observations across the full GW spectrum provided by LISA in the milli-Hz band, B-DECIGO in the deci-Hz band, and aLIGO and ET in the hecto-Hz, looking at two specific aspects of the multiband GW astronomy/physics: parameter estimation errors and tests of GR.

We begin in Section 2 by providing a set of our basic tools for the signal analysis in the matched filtering technique: i) the noise PSD in Section 2.1; ii) the GW signal models in Sections 2.2 and 2.3; and iii) the multiband Fisher matrix formalism in Section 2.4. In Section 3, we present the parameter estimation errors of GW190521-like non-precessing, quasicircular BBH systems using the multiband GW observations. They are displayed in Table 2 and 3. Based on the estimated errors, we then examine in Section 4 what extent the future multiband observation of GW190521-like BBH system will improve tests of GR; this includes an inspiral–ringdown consistency test (see Table 4), and a simple test to discriminate between the remnant BH based on GR and other remnant compact objects (see Figure 2), which may allow to prove the ergoregion of Kerr geometry shown in Figure 3. We conclude in Section 5 with complications and various effects, which are not covered in this paper due to our assumptions and simplifications.

Appendices contain some additional analysis and information. While the quasicircular BBH merger is the most favored scenario by the LIGO/Virgo analysis [3,4], other alternative scenario such as an eccentric BBH merger may also be consistent with the observed source for GW190521 [44]. We briefly discuss the multiband visibility of GW190521-like eccentric BBH in Appendix A. Also, additional noise PSD of ground/space-based, current/future GW detectors is provided in Appendix B, as a complement of our treatment in Section 2.1.

Throughout this paper, the binary parameters and GW frequencies measured in the source’s rest frame are denoted with the index ‘r’, explicitly distinguished from those in the observer frame.

## 2. Method for signal-to-noise ratio and Fisher analysis

In this section, we summarize our methodology of multiband GW data analysis in the specific context of a non-precessing, spinning, quasicircular GW190521-like BBH system, where the spins are aligned to the orbital angular momentum; an alternative scenarios of non-zero orbital eccentricity in GW190521-like BBH system will be discussed in Appendix A. Our simple framework here is largely based on the previous B-DECIGO works [9,38].

### 2.1. aLIGO, ET, B-DECIGO and LISA

For our multiband GW observation, we follow Ref. [38] by considering the four GW observatories: aLIGO and ET in the hecto-Hz band, B-DECIGO in the deci-Hz, and LISA in the milli-Hz band (see also Appendix B for some of other GW detectors in these bands). It should be noted that we shall treat the “non sky-averaging” PSD  $S_n(f)$ ; we will account for the average over the GW detector’s antenna pattern function at the level of the waveform.

For aLIGO in the hecto-Hz band, we use Eq. (4.7) in Ref. [45],

$$S_n^{\text{aLIGO}} = 10^{-48} \left( 0.0152 x^{-4} + 0.2935 x^{9/4} + 2.7951 x^{3/2} - 6.5080 x^{3/4} + 17.7622 \right) \text{ Hz}^{-1};$$

$$x = \frac{f}{245.4 \text{ Hz}}.$$
 (4)

For a 3rd generation (3G) GW interferometer: ET in the hecto-Hz band, we find Table 1 in Ref. [46] as

$$S_n^{\text{ET}} = 1.5 \times 10^{-52} \left( y^{-4.1} + 186.0 y^{-0.69} \right. \\ \left. + 233.0 \times \frac{1.0 + 31.0 y - 65.0 y^2 + 52.0 y^3 - 42.0 y^4 + 10.0 y^5 + 12.0 y^6}{1.0 + 14.0 y - 37.0 y^2 + 19.0 y^3 + 27.0 y^4} \right) \text{ Hz}^{-1};$$

$$y = \frac{f}{200.0 \text{ Hz}}.$$
 (5)

For B-DECIGO in the deci-Hz band, we use Eq. (20) in Ref. [38], originally proposed by Nakamura et al. [9]:

$$S_n^{\text{BD}} = \left[ (2.01 \times 10^{-23})^2 + \left( \frac{2.53 \times 10^{-18}}{F^2} \right)^2 + (8.00 \times 10^{-22} F)^2 \right] \text{ Hz}^{-1};$$

$$F = \frac{f}{1.0 \times 10^{-3} \text{ Hz}}.$$
 (6)

For LISA in the milli-Hz band, we use Eq. (1) of in Ref. [47], which is based on the 2018 LISA Phase-0 reference design parameters. Discarding the galactic confusion noise for simplicity, it reads<sup>3</sup>

$$S_n^{\text{LISA}} = \left( 2.4602 \times 10^{-41} + 4.0504 \times 10^{-38} z^2 + \frac{4.7850 \times 10^{-48}}{z^2} \right. \\ \left. + \frac{2.8485 \times 10^{-51}}{z^4} + \frac{3.9412 \times 10^{-58}}{z^6} \right) \text{ Hz}^{-1};$$

$$z = \frac{f}{1.0 \text{ Hz}}.$$
 (7)

### 2.2. Waveform models

We employ as our BBH waveform model the frequency-domain, “restricted” waveform in the stationary phase approximation for the inspiral phase, and the frequency-domain, single-mode waveform for the ringdown phase. We shall restrict our waveform model to these two phases to simplify our

---

<sup>3</sup> Our expression  $S_n^{\text{LISA}}$  (7) is smaller than Eq.(1) in Ref. [47] by a overall factor of 5; the difference arises simply because Eq. (7) does not account for the sky-averaging.

analysis as far as possible; the complete IMR treatment at the level of waveform (using, for example, Effective-one-body approach [48] and IMRPhenom model [49]) will be left for future work.

The GW waveform from a BBH inspiral in the frequency domain has the well-known form (see, for example, Ref. [50])

$$\tilde{h}_{\text{Insp}}(f) = \mathcal{A} f^{-7/6} e^{i\Psi_{\text{Insp}}(f)}, \quad (8)$$

where  $\mathcal{A}$  is the ‘‘Newtonian’’ amplitude averaging over all sky positions and binary orientations (see, for example, Ref. [51]), so that

$$\mathcal{A} \equiv \frac{2}{5} \sqrt{\frac{5}{24}} \pi^{-2/3} \frac{\mathcal{M}^{5/6}}{D_L}. \quad (9)$$

The waveform’s frequency-domain phase  $\Psi_{\text{Insp}}(f)$  in the post-Newtonian (PN) approximation is given by (see, for example, Ref. [52])

$$\Psi_{\text{Insp}}(f) = 2\pi f t_c - \Psi_c - \frac{\pi}{4} + \frac{3}{128\nu^5} \left( \Delta\Psi_{3.5\text{PN}}^{\text{PP}} + \Delta\Psi_{3.5\text{PN}}^{\text{PP-spin}} + \Delta\Psi_{3.5\text{PN}}^{\text{BH-tidal}} \right), \quad (10)$$

where  $\nu \equiv (\pi m_t f)^{1/3}$  is the PN parameter (in terms of the observer-frame total mass), and  $t_c$  and  $\phi_c$  are the time and phase at coalescence. The phase terms  $\Delta\Psi_{3.5\text{PN}}^{\text{PP}}$  and  $\Delta\Psi_{3.5\text{PN}}^{\text{PP-spin}}$  are the 3.5PN spin-independent, point-particle contributions derived in Ref. [53] and the 3.5PN spin-dependent, point-particle contributions that include linear spin-orbit [54,55], quadratic-in-spin [56] and cubic-in-spin [57] effects, respectively. The remaining phase term  $\Delta\Psi_{3.5\text{PN}}^{\text{BH-tidal}}$  is related to the tidal response of a spinning BH as a finite-size body, i.e., BH-absorption corrections such as the GW energy and angular momentum fluxes down to the horizons and the associated evolution of the BH itself [58–60].

Meanwhile, limited to only fundamental ( $n = 0$ ),  $\ell = 2 = m$  modes, the time-domain, single-mode ringdown waveform measured at a GW observatory is written as [61,62]

$$h_{\text{Ring}}(f_c, Q, t_0, \phi_0; t) = \begin{cases} e^{-\frac{\pi f_c (t-t_0)}{Q}} \cos[2\pi f_c (t-t_0) - \phi_0] & \text{for } t \geq t_0, \\ 0 & \text{for } t < t_0, \end{cases} \quad (11)$$

where  $t_0$  and  $\phi_0$  are the initial time and phase of the ringdown, respectively, and we have ignored the overall amplitude so that Eq. (11) is not normalized; the initial ringdown amplitude may be determined by matching the ringdown GW waveform to the merger one (refer to, for example, Eq. (16) below). When the final remnant object is a Kerr BH, the central frequency  $f_c$  and the quality factor  $Q$  are given in terms of QNM frequencies ( $f_{\text{QNM}} = f_{\text{R}} + i f_{\text{I}}$ ) of the remnant BH as [see Eq. (7) of Ref. [63]]

$$f_c := f_{\text{R}}, \quad Q := -\frac{f_{\text{R}}}{2f_{\text{I}}}. \quad (12)$$

It should be noted that  $f_{\text{QNM}} = f_{\text{QNM}}^{\text{f}}(1+z)^{-1}$  here is given in the observer frame. The Fourier transforms of Eq. (11) provide the corresponding frequency-domain waveform, which takes the form (here we follow the convention of Ref. [61])

$$\tilde{h}_{\text{Ring}}(f_c, Q, t_0, \phi_0; f) = \frac{Q(f_c \cos \phi_0 - 2iQf \cos \phi_0 + 2Qf_c \sin \phi_0)}{\pi(f_c + 2iQf_c - 2iQf)(f_c - 2iQf_c - 2iQf)} e^{2i\pi f t_0}. \quad (13)$$

We note that this frequency-domain GW waveform is not normalized, too <sup>4</sup>, following the approach presented in Appendix B of Ref. [62].

The ringdown waveforms (11) and (13) require input data for the QNM frequency of the final remnant BH. Because we do not consider the complete IMR phase at the level of waveform, we employ the numerical-relativity (NR) remnant fitting formulas (see, for example, Refs. [65–70] and references therein), from which the final  $M_f$  and spin  $\mathbf{S}_f$  of the remnant BH are consistently inferred for a given initial BH masses  $m_{1,2}$  and dimensionless spin parameters  $\vec{\chi}_{1,2}$  (in the inspiral phase) as

$$M_f = M_f(m_1, m_2, \vec{\chi}_1, \vec{\chi}_2), \quad \chi_f \equiv \frac{|\mathbf{S}_f|}{M_f^2} = \chi_f(m_1, m_2, \vec{\chi}_1, \vec{\chi}_2). \quad (14)$$

We then generate the accurate numerical data of  $f_{\text{QNM}}$  of the inferred remnant BH with the Black Hole Perturbation Club (B.H.P.C.) code [71] to obtain  $f_c$  and  $Q$  <sup>5</sup>. In practice, it is also convenient to present  $f_c$  and  $Q$  by means of a compact analytical formula. Such a formula for the ( $\ell = 2, m = 2, n = 0$ ) mode is obtained in Ref. [76] (by performing fits to the numerical QNM frequency data), and it reads

$$f_c = \frac{1}{2\pi M_f} \left[ f_1 + f_2 (1 - \chi_f)^{f_3} \right], \quad Q = q_1 + q_2 (1 - \chi_f)^{q_3}, \quad (15)$$

with  $f_1 = 1.5251, f_2 = -1.1568, f_3 = 0.1292, q_1 = 0.7000, q_2 = 1.4187$  and  $q_3 = -0.4990$ .

### 2.3. Signal-to-noise ratio

We estimate the SNR of a complete IMR GW signal, making use of the simple frequency-domain, IMR “amplitude” model [9]. This model is motivated by the waveform amplitude in the IMRPhenomB model [77] and it is given by

$$\text{IMR}(f) = \mathcal{A} \times \begin{cases} f^{-7/6} & \text{for } f < f_{\text{max}}, \\ f_{\text{max}}^{-1/2} f^{-2/3} & \text{for } f_{\text{max}} \leq f < f_{\text{R}}^{\text{r}}/(1+z), \\ \frac{f_{\text{max}}^{-1/2} [f_{\text{R}}^{\text{r}}/(1+z)]^{-2/3} [f_{\text{I}}^{\text{r}}/(1+z)]^2}{\{f - [f_{\text{R}}^{\text{r}}/(1+z)]\}^2 + [f_{\text{I}}^{\text{r}}/(1+z)]^2} & \text{for } f_{\text{R}}^{\text{r}}/(1+z) \leq f, \end{cases} \quad (16)$$

where the overall constant  $\mathcal{A}$  is chosen to be the (averaged) GW signal’s amplitudes in the inspiral phase (9). We set  $f_{\text{max}} = 1/[6^{3/2}\pi(1+z)m_i^{\text{r}}]$  as the GW frequency at the innermost stable circular orbit (ISCO) of a test particle in the Schwarzschild spacetime with the total mass of BBH  $m_i^{\text{r}}$ , and  $f_{\text{R}}^{\text{r}}$  and  $f_{\text{I}}^{\text{r}}$  are the real and imaginary parts of the QNM frequency (i.e.,  $f_{\text{QNM}}^{\text{r}} = f_{\text{R}}^{\text{r}} + i f_{\text{I}}^{\text{r}}$ ) of the fundamental ( $n = 0$ ),  $\ell = 2 = m$  mode, which are determined by the final mass and spin of the remnant BH; the redshift dependence appears because the model parameters ( $m_i^{\text{r}}, f_{\text{R}}^{\text{r}}, f_{\text{I}}^{\text{r}}$ ) are all given in the source’s rest frame (while the GW

<sup>4</sup> The maximized SNR over the initial ringdown phase  $\phi_0$  has been discussed in Ref. [64].

<sup>5</sup> For accurate numerical data of  $f_{\text{QNM}}$ , see also Ref. [72], Emanuele Berti’s “Ringdown” website [73], Ref. [74] and the Black Hole Perturbation Toolkit [75].

frequencies  $f$  and  $f_{\max}$  are in the observer frame). The averaged SNR (in the above sense) can be then obtained by <sup>6</sup>

$$\rho_{\text{ave}} = 2 \left\{ \int_{f_{\text{in}}}^{f_{\text{end}}} \frac{[\text{IMR}(f)]^2}{S_n(f)} df \right\}^{1/2}, \quad (17)$$

where  $S_n(f)$  is the noise PSD, and the frequency range  $[f_{\text{in}}, f_{\text{end}}]$  is determined by the GW detector with which we observe the GW signals.

Note that the amplitude spectral density (i.e., the square root of the PSD of the source amplitudes) is  $\sqrt{S_h(f)} \equiv 2\sqrt{f} |\text{IMR}(f)|$  in this model, and its track for the GW190521-like BBH is plotted in Figure 1 with the (square root of) the noise PSD  $\sqrt{S_n(f)}$ , assuming the median values of Table 1 and the remnant formulas of Ref. [65].

#### 2.4. Multiband Fisher analysis

We approximate the variance (uncertainty squared) associated with the measurement of a set of signal parameters, making use of the standard Fisher matrix formalism. The Fisher information matrix for a single-band GW detector is defined by

$$\Gamma_{ab} \equiv \left( \frac{\partial \tilde{h}}{\partial \theta_a} \middle| \frac{\partial \tilde{h}}{\partial \theta_b} \right) \bigg|_{\theta=\theta_0}, \quad (18)$$

where  $\tilde{h}(f, \theta)$  is the frequency-domain GW signal described by the set of parameters  $\theta$ ,  $\theta_0$  is the best-fit values of the binary parameters. The bracket defines the noise-weighted inner product over the frequency range of  $[f_{\text{in}}, f_{\text{end}}]$  [79]

$$(a | b) \equiv 2 \int_{f_{\text{in}}}^{f_{\text{end}}} \frac{\tilde{a}^*(f) \tilde{b}(f) + \tilde{b}^*(f) \tilde{a}(f)}{S_n(f)} df, \quad (19)$$

with asterisk ‘\*’, denoting the complex conjugation. The inverse Fisher matrix defines the corresponding variance-covariance matrix  $\Sigma^{ab} \equiv (\Gamma_{ab})^{-1}$ . In the limit of suitable high SNR [80], the variance of the parameter  $\theta^a$  are then given by

$$\sigma_a^2 = \Sigma^{aa}. \quad (20)$$

In the case of the multiband analysis (to combine the information from, for example, aLIGO + B-DECIGO), we simply construct a multiband SNR and Fisher matrix by adding individual (averaged) SNRs and Fisher information matrices for each GW detector:

$$\rho_{\text{tot}}^2 \equiv \sum_I (\rho_{\text{ave}}^I)^2, \quad \Gamma_{ab}^{\text{tot}} \equiv \sum_I \Gamma_{ab}^I, \quad (21)$$

<sup>6</sup> For the given Fourier transform of a GW signal  $\tilde{h}(f)$ , the SNR can be written in terms of either  $\tilde{h}(f)$  itself with the dimension of 1/Hz, the spectral density of the source amplitude is  $\sqrt{S_h(f)} \equiv 2\sqrt{f} |\tilde{h}(f)|$  with the dimension of 1/ $\sqrt{\text{Hz}}$ , or the dimensionless characteristic strain  $h_c(f) \equiv 2f |\tilde{h}(f)|$  [78].

$$\rho_{\text{ave}} = \left( \int_{f_{\text{in}}}^{f_{\text{end}}} \frac{|2\tilde{h}(f)|^2}{S_n(f)} df \right)^{1/2} = \left( \int_{f_{\text{in}}}^{f_{\text{end}}} \frac{|\sqrt{S_h(f)}|^2}{S_n(f)} \frac{df}{f} \right)^{1/2} = \left( \int_{f_{\text{in}}}^{f_{\text{end}}} \frac{[h_c(f)]^2}{f S_n(f)} \frac{df}{f} \right)^{1/2}.$$



where  $\rho_{\text{ave}}^I$  and  $\Gamma_{ab}^I$  are the averaged SNR and the Fisher matrix for the  $I$ -th detector. The multiband variance-covariance matrix is defined by

$$\Sigma_{\text{tot}}^{ab} \equiv (\Gamma_{ab}^{\text{tot}})^{-1}, \quad (22)$$

and the variance of  $\theta^a$  is then obtained by  $\sigma_a^2 = \Sigma_{\text{tot}}^{aa}$ .

### 3. Parameter estimation errors via multiband observation

In this section, we summarize the parameter estimation errors for a non-precessing, spinning, GW190521-like BBH system, using the multiband GW network (LISA, B-DECIGO, aLIGO and ET) detailed in Section 2.1. We follow Refs. [38,63] in our treatment of the Fisher matrix calculation for BBH GW signals<sup>7</sup>, and we continue to neglect the contribution from the merger GW signal.

#### 3.1. Setup of Fisher analysis

We set the default frequency interval of each GW detector  $[f_{\text{low}}, f_{\text{up}}]$  as  $[10.0, 3.0 \times 10^3]$  Hz (aLIGO),  $[2.0, 3.0 \times 10^3]$  Hz (ET),  $[0.01, 1.0 \times 10^2]$  Hz (B-DECIGO), and  $[1.0 \times 10^{-4}, 1.0]$  Hz (LISA), respectively. We shall adopt the  $T_{\text{obs}} = 5$ -year observations time, and assume that the binary merges at the GW frequency of the Schwarzschild ISCO,  $f_{\text{ISCO}} = 1/[6^{3/2}\pi(1+z)m_1^*]$ . In this setup, the minimum frequency of the GW signal is

$$f_{\text{min}} = 9.24 \times 10^{-3} (1+z)^{-5/8} \left( \frac{\mathcal{M}^r}{65.1 M_{\odot}} \right)^{5/8} \left( \frac{5 \text{ yr}}{T_{\text{obs}}} \right)^{3/8} \text{ Hz}, \quad (23)$$

where  $\mathcal{M}^r$  is the chirp mass in the source's rest frame, normalized to that of GW190521. Therefore, the GW signals observed by each GW detector is truncated at the corresponding initial frequency  $f_{\text{in}} \equiv \max(f_{\text{min}}, f_{\text{low}})$  as well as the end frequency  $f_{\text{end}} \equiv \min(f_{\text{ISCO}}, f_{\text{up}})$ ; recall Figure 1.

The parameters of the inspiral waveform (8) are

$$\theta_{\text{Insp}} = (f_0, t_c, \Psi_c, \ln m_t, \nu, \chi_s, \chi_a), \quad (24)$$

where  $f_0 = 1.65$  Hz at which B-DECIGO is most sensitive, and we define the symmetric and anti-symmetric combinations of BH spins by  $\chi_s \equiv (\chi_1 + \chi_2)/2$  and  $\chi_a \equiv (\chi_1 - \chi_2)/2$  with the component (aligned) BH spins  $\chi_{1,2} \equiv |\vec{\chi}_{1,2}| \equiv |\mathbf{S}_{1,2}|/m_{1,2}^2$ . At the same time, the parameters of the ringdown waveform (13) are

$$\theta_{\text{Ring}} = (t_0, \phi_0, f_c, Q). \quad (25)$$

It should be noted that the amplitude parameters are left out from the set of our independent parameters both in Eqs. (24) and (25). They are entirely uncorrelated with other parameters  $\theta_a$  because the variance-covariance matrix  $\Sigma^{ab}$  gives the variance  $\sigma_{\ln \mathcal{A}}^2 = \rho_{\text{ave}}^{-2}$  and the correlation  $c^{\ln \mathcal{A}, a} \equiv \Sigma^{\ln \mathcal{A}, a} / (\sigma_{\ln \mathcal{A}} \sigma_a) = 0$  for the inspiral GW signals (8) (see, for example, Ref. [82]), and similar for the ringdown GW signals (if we explicitly introduce the amplitude to the normalized waveform of Eq. (13)). For simplicity, we consider that all (other) parameters are unconstrained.

<sup>7</sup> The setup here is slightly different from Ref. [38]; i) we will assume the 5 yr observation, rather than 4 yr observation, and ii) we will use the new LISA sensitivity curve proposed by Ref. [47] and displayed in Eq. (7), not the earlier eLISA sensitivity curve presented in Ref. [81].

The best fit parameters values of the inspiral GW signal are given by the median values in Table 1 with  $t_c = 0.0 = \Psi_c$ , while those of the ringdown GW signal are assumed to be  $\phi_0 = 0.0 = t_0$ <sup>8</sup>, and

$$(f_c, Q) = (85.061 \text{ Hz}, 4.8354), \quad (26)$$

for the (observer-frame) central frequency and quality factor. The values in Eq. (26) are obtained via Eq. (12) for a given QNM frequency data of the remnant BH, assuming that the remnant mass  $M_f$  and spin  $\chi_f$  of the final BH are inferred via the remnant formula in Eq. (14) with the parameters of each component BH in Table 1. Specifically, we use the remnant formula provided by Ref. [68], and we quote<sup>9</sup>

$$\left(\frac{M_f}{m_t}, \chi_f\right) = (0.90356, 0.88269). \quad (27)$$

The associated QNM frequency data of this remnant BH is then generated by the B.H.P.C. code [71], yielding the results in Eq. (26).

To see the benefit of the multiband GW observation, finally, we introduce the normalized root-mean-square errors as

$$\delta\hat{\theta} \equiv \rho \sigma, \quad (28)$$

and shall display our error estimations in terms of  $\delta\hat{\theta}$  with the total averaged SNR  $\rho_{\text{ave}}^{\text{tot}}$  accumulated over multibands.

### 3.2. Result: Inspiral phase

In Table 2, we present the parameter estimation errors of mass parameters ( $m, \nu$ ) and spin parameters ( $\chi_s, \chi_a$ ) for the GW190521-like BBH inspiral in various combinations of ground/space-based GW observatories (but suppressing those of  $t_c$  and  $\Psi_c$ ). Here, it should be noted that only the inspiral phase is analyzed here, and the merger–ringdown phase which contributes to the SNR for ground-based observatories, is ignored. Therefore, the SNR for aLIGO quoted here is much smaller than the observed LIGO/Virgo network SNR of 14.5 [3].

In the single-band case, as seen in Figure 1, the inspiral GW signal of GW190521-like BBHs are best observed by B-DECIGO because it can cover both the early (1 yr before merger) and late (around the ISCO) phases. However, B-DECIGO observation alone does not enough benefit to discern the spin parameters. Also, interestingly, the normalized errors of LISA observation is better than those of ET. Although the SNR of LISA is one order of magnitude smaller than that of B-DECIGO and ET (and it would be actually too small compared to the ‘realistic’ detection SNR threshold of  $\sim 15$  [83]), the longer observation period ( $\sim$  years) can reduce the normalized uncertainty.

In the multiband cases, thanks to the wider bandwidth, the observation with B-DECIGO and ET gives a factor of 2 improvement in all the parameter estimation, even if we observe only the inspiral GW signal. This is further refined if we combine the data from LISA, forming a triple-band network. Our result therefore shows that the multibanding the LISA, B-DECIGO and ET observatories would be only viable

<sup>8</sup> The parameter estimation errors are independent of the value of the initial time  $t_0$ . In our frequency-domain, single-mode ringdown waveform in Eq. (13), the  $t_0$  dependence is factorized as  $e^{2i\pi f t_0}$  and it does not contribute to the noise-weighted inner product in Eq. (19). On the other hand, the estimation errors depend on the initial phase  $\phi_0$  weakly [62].

<sup>9</sup> These values are (marginally) consistent with the final mass and spin reported in the LIGO/Virgo GW190521 detection paper [3]. Recall that we have assumed that the individual spins of GW190521-like BBH are non-precessing, and completely aligned to the orbital angular momentum.

network to measure all the binary parameters of GW190521-like BBH system, including BH's component spins.

**Table 2.** Parameter estimation errors of mass parameters ( $m, \nu$ ) and spin parameters ( $\chi_s, \chi_a$ ) for GW190521-like quasicircular BBH inspiral, normalized to the total multiband SNR  $\rho_{\text{tot}}$ ; for example, the result of “BD” in “BD + aLIGO” is normalized to  $\rho_{\text{tot}} = 5.93 \times 10^1$ . We assume that the true binary parameters are given by the median values of Table 1, i.e.,  $m_t = 151.0 M_\odot$ ,  $\nu = 0.246$ ,  $\chi_s = 0.71$  and  $\chi_a = 0.02$ . Since the source location can be determined well by B-DECIGO (BD here) [9,39], we fix  $1 + z = 1.82$ . Note that only the inspiral SNR of aLIGO is 1.76, which is too small to give meaningful estimation errors. Also any estimation errors  $\delta\hat{\theta} > 1.0 \times 10^6$  are discarded from this table.

GW detector	SNR	$\delta\hat{m}_t/m_t$	$\delta\hat{\nu}/\nu$	$\delta\hat{\chi}_s/\chi_s$	$\delta\hat{\chi}_a/\chi_a$
BD + aLIGO					
BD	$5.92 \times 10^1$	$3.51 \times 10^{-1}$	$5.84 \times 10^{-1}$	4.91	$1.12 \times 10^3$
aLIGO	1.76	...	...	...	...
BD + aLIGO	$5.93 \times 10^1$	$3.44 \times 10^{-1}$	$5.73 \times 10^{-1}$	4.73	$1.08 \times 10^3$
BD + ET					
ET	$2.72 \times 10^1$	$3.70 \times 10^2$	$6.00 \times 10^2$	$5.86 \times 10^3$	...
BD + ET	$6.52 \times 10^1$	$2.88 \times 10^{-1}$	$4.80 \times 10^{-1}$	3.07	$7.01 \times 10^2$
LISA + BD + ET					
LISA	2.68	$1.73 \times 10^1$	$2.89 \times 10^1$	$2.37 \times 10^3$	...
LISA + BD	$5.93 \times 10^1$	$1.83 \times 10^{-1}$	$3.04 \times 10^{-1}$	4.01	$9.11 \times 10^2$
LISA + BD + ET	$6.52 \times 10^1$	$1.45 \times 10^{-1}$	$2.41 \times 10^{-1}$	2.52	$5.71 \times 10^2$

### 3.3. Result: Ringdown phase

In Table 3, we show the parameter estimation errors of the central frequency  $f_c$  and quality factor  $Q$  (but suppressing those of  $t_0$  and  $\phi_0$ ) for the ringdown phase of GW190521-like BBH in ground-based observatories. For simplicity, we estimate the ringdown amplitude and associated SNR via the IMR amplitude model in Eq. (16)<sup>10</sup>. We see that ET will be able to measure QNM frequency with the statistical error  $\sim 10^{-3}$ . At the same time, however, the difference in the normalized errors  $\delta\hat{f}_c$  and  $\delta\hat{Q}$  between aLIGO and ET observations are not so evident. We speculate it arises from the difference in the spectrum shapes (not the overall amplitudes) because the ringdown waveform (13) is narrow-banded in the frequency domain.

**Table 3.** Parameter estimation errors of the central frequency  $f_c$  and the quality factor  $Q$  of GW190521-like BBH, only using the ringdown GW signal. The errors are normalized to the SNR of each corresponding observatories.

GW detector	SNR	$\delta\hat{f}_c/f_c$	$\delta\hat{Q}/Q$
aLIGO	$1.08 \times 10^1$	$3.42 \times 10^{-1}$	$2.71 \times 10^{-1}$
ET	$1.47 \times 10^2$	$3.66 \times 10^{-1}$	$2.86 \times 10^{-1}$

<sup>10</sup> We should note that this approximation is likely too raw because the ringdown amplitude strongly depends on the starting time  $t_0$  of the ringdown phase, which is difficult to determine in practice.

#### 4. The implications for tests of GR via multiband observation

In this section, we explore what extent the multiband observation of GW190521-like BBH system discussed in Section 3 could improve tests of GR. A handful of tests have been already formulated and performed with merging BBH systems (see, for example, Refs. [84–87]), and we follow the (very) simple tests proposed by Nakano et al. [63,88].

##### 4.1. A consistency test of GR with the inspiral and ringdown GW signals

One possible test of GR with a BBH system is to establish the consistency of the mass and spin of the final remnant BH determined by two different parts of the GW signals. Thanks to the recent advancement in NR simulations of BBH systems [89–91] (see also Refs. [92–96]), one can infer these values from the initial component masses and spins measured from the inspiral GW signals (in the low-frequency band), making use of the NR fitting formulas for the remnant properties of the final BH; recall Section 2.2. At the same time, they are directly estimated from the succeeding merger–ringdown GW signal (in the high-frequency band). This type of test is now known as the “IMR consistency test” [97,98]. By formulation, multiband observations of heavy BBH mergers such as GW190521-like BBH systems will be “golden binaries” [99] of such an IMR consistency test.

Given that the early inspiral and late ringdown GW signals will be best observed in a different frequency band (such as “B-DECIGO + aLIGO” network etc.), we here perform the multiband version of the “inspiral–ringdown (IR) test” formulated by Nakano et al. [63] (see also Refs. [99,100]), solely using the inspiral and ringdown parts, and test the consistency of GR across the merger part, which is highly dynamical phase in a strong-field regime. We estimate the statistical errors on  $M_f$  and  $\chi_f$  from the inspiral GW signal by using the (normalised) statistical errors  $\delta\hat{\theta}$  in Table 2 and applying a standard variance propagation of non-linear functions to the specific NR remnant formulas (“UIB formulas”) [68] publicly available in LALInference [101,102]<sup>11</sup>. The errors from the ringdown GW signal are estimated from Table 3, through the dependence of  $f_c$  and  $Q$  on  $(M_f, \chi_f)$ <sup>12</sup>.

In Table 4, we present the parameter estimation errors of the remnant mass  $M_f$  and spin  $\chi_f$  from both the inspiral and ringdown phases. For the reference, we also present the same errors of GW150914-like BBH with the redshifted component masses  $(m_1, m_2) = (30 M_\odot, 40 M_\odot)$ , the component spin magnitudes  $(\chi_1, \chi_2) = (0.9, 0.7)$ , and the luminosity distance  $D_L = 0.4$  Gpc (i.e., the redshift  $z \sim 0.085$ )<sup>13</sup>. We see that multiband “LISA + B-DECIGO + ET” allows us the IMR consistency test at the sub-percent precision both for GW150914-like, and GW190521-like BBH systems. The result of GW190521-like BBH system is slightly worse than the case of GW150914-like BBH system because the luminosity distance of GW190521 ( $D_L = 5.3$  Gpc) is much larger than that of GW150914 ( $D_L = 0.4$  Gpc) [22,103,104]. Also, the GW190521-like BBH system has the central frequency  $f_c \sim 85$  Hz lower than that of the GW150914-like BBH system ( $f_c \sim 350$  Hz), missing the most sensitive frequency of aLIGO and ET  $\sim 250$  Hz. If a GW190521-like BBH was observed at the same distance as GW150914, the accuracy of its IMR consistency test would be at the level of  $\sim O(0.01\%)$ .

<sup>11</sup> We ignore the systematic bias due to our specific choice of the NR remnant formulas, for simplicity. See, for example, Refs. [95,98] for details.

<sup>12</sup> Technically, this procedure requires the evaluation of the partial derivatives  $(\partial f_c / \partial \chi_f)_{M_f}$  etc. to compute the variance propagation. We construct the numerical function of QNM frequencies  $M_f f_{\text{QNM}}(\chi_f)$  with the B.H.P.C. code [71] around the best fit values of Eq. (27), from which these derivatives are extracted.

<sup>13</sup> This system was analyzed as “System B” in Ref. [38].

**Table 4.** Parameter estimation errors of the remnant mass and spin of GW190521-like and GW150914-like BBH systems, using only the ringdown GW signal as well as the inspiral GW signal inferred via the NR remnant fitting formulas; the best fit values  $(M_f/m, \chi_f) \sim (0.904, 0.883)$  for the GW190521-like BBH (recall Eq. (27)) and  $(M_f/m, \chi_f) \sim (0.891, 0.898)$  for the GW150914-like BBH. Here, BD is an abbreviation for B-DECIGO. The results in the single band are normalized to the SNR for a given GW observatory. In the multiband case they are normalized to the total SNR of  $\rho_{\text{LISA+BD+ET}}$ .

GW detector	GW190521-like BBH			GW150914-like BBH		
	SNR	$\delta M_f/M_f$	$\delta \chi_f/\chi_f$	SNR	$\delta M_f/M_f$	$\delta \chi_f/\chi_f$
Single band: Ringdown GW signal						
aLIGO	$1.08 \times 10^1$	$3.09 \times 10^{-1}$	$7.47 \times 10^{-1}$	$1.78 \times 10^1$	$3.05 \times 10^{-1}$	$6.47 \times 10^{-1}$
ET	$1.47 \times 10^2$	$3.31 \times 10^{-1}$	$7.90 \times 10^{-1}$	$2.66 \times 10^2$	$3.26 \times 10^{-1}$	$6.60 \times 10^{-1}$
Single band: inspiral GW signal						
BD	$5.92 \times 10^1$	$3.31 \times 10^{-1}$	$9.63 \times 10^{-1}$	$2.51 \times 10^2$	$3.19 \times 10^{-1}$	$9.43 \times 10^{-1}$
Multiband: inspiral GW signal						
BD + ET	$6.52 \times 10^1$	$3.55 \times 10^{-1}$	$5.91 \times 10^{-1}$	$5.18 \times 10^2$	$1.07 \times 10^{-1}$	$4.48 \times 10^{-1}$
LISA + BD	$5.93 \times 10^1$	$2.46 \times 10^{-1}$	$8.05 \times 10^{-1}$	$2.51 \times 10^2$	$6.39 \times 10^{-1}$	1.85
LISA + BD + ET	$6.52 \times 10^1$	$1.75 \times 10^{-1}$	$4.98 \times 10^{-1}$	$5.18 \times 10^2$	$1.06 \times 10^{-1}$	$4.33 \times 10^{-1}$

#### 4.2. A simple test of the remnant compact object with quasinormal modes

Another simple test of GR is to bracket whether the remnant object should be a BH predicted by GR or not, making use of the parameter estimation errors of quasinormal mode (QNM) frequencies ( $f_{\text{QNM}} = f_{\text{R}} + i f_{\text{I}}$ ) obtained from the ringdown GW signals [63].

Figure 2 plots the  $1\sigma$ ,  $2\sigma$ ,  $3\sigma$ ,  $4\sigma$ , and  $5\sigma$  error contours on the fundamental ( $n = 0$ ),  $\ell = 2 = m$  mode of the QNM frequency in the  $(f_{\text{R}}, f_{\text{I}})$  plane, in the case of GW190521-like BBH system observed by aLIGO (left) and ET (right). The errors are estimated through the results in Table 3 about the parameter estimation error on the ringdown GW signal (after  $t_0$  and  $\phi_0$  being marginalized out), and the outermost contour in each panel shows the  $5\sigma$  error. This black lines in each panels depict the Schwarzschild limit of  $|f_{\text{I}}|/f_{\text{R}}$ , which may be obtained by setting  $\chi_f = 0$  in Eq. (15) with Eq. (12)<sup>14</sup>,

$$\frac{|f_{\text{I}}|}{f_{\text{R}}} \approx 0.236. \quad (29)$$

The key point of this test is that the top-left side of the black line becomes the prohibited region in GR, i.e., for the ( $n = 0$ ),  $\ell = 2 = m$  mode, the QNM frequencies  $(f_{\text{R}}, f_{\text{I}})$  of any rotating Kerr BHs must sit in the bottom-right side of the black line.

In the aLIGO case, due to the low SNR ( $= 10.8$ ), the parameter estimation errors already go beyond the Schwarzschild limit at the  $3\sigma$  level, and we cannot confirm whether the remnant object is a BH predicted by GR with the  $5\sigma$  level. For such low SNR events, the ‘‘coherent mode stacking method’’ [105] will be useful. On the other hand, thanks to the the high SNR ( $= 147$ ) in the ET case, this simple test can necessarily confirm that the remnant object is a GR-predicted BH<sup>15</sup>.

<sup>14</sup> This is marginally consistent with the exact QNM frequency of the fundamental ( $n = 0$ ),  $\ell = 2 = m$  mode in the Schwarzschild limit. For example, the B.H.P.C. code gives  $|f_{\text{I}}|/f_{\text{R}} = 0.23808\dots$ , and the difference is negligibly small for our raw analysis here.

<sup>15</sup> The  $(M_f, \chi_f)$  plane has been discussed as Figure 5 in Ref. [3]. The remnant BH spin is restricted to  $0 \leq \chi_f < 1$  in the analysis. Therefore, the simple test presented in this paper is not applicable.

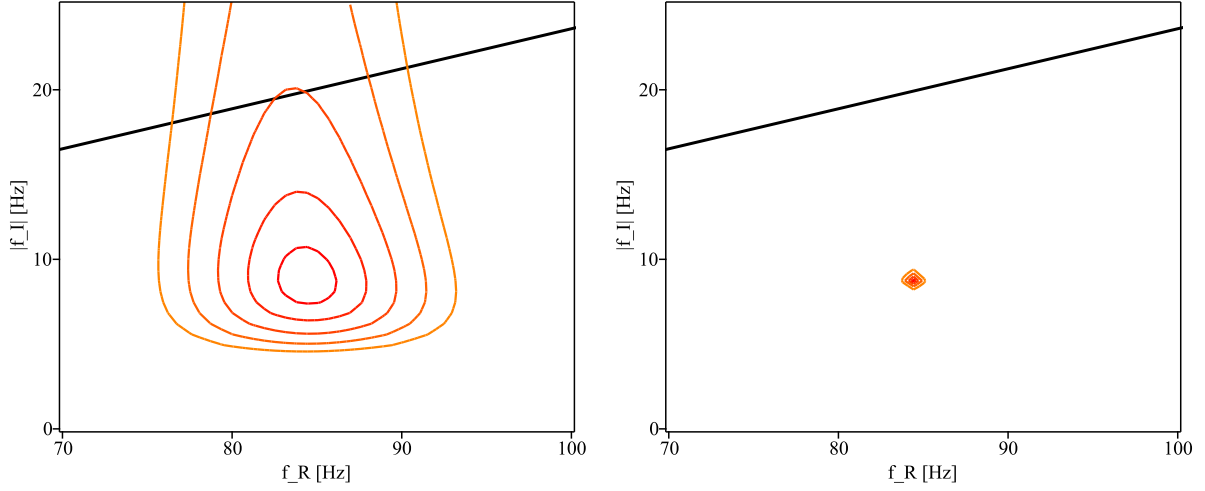


**Figure 2.** Simple remnant test in the  $(f_R, f_I)$  plane. The QNM frequency is given in the observer frame, and we assume the GW190521-like ringdown GW signals with  $(M_f/m, \chi_f) \sim (0.904, 0.883)$  (27). The figure shows the parameter estimation error with the aLIGO noise curve (left,  $\text{SNR} = 1.08 \times 10^1$ ) and the ET one (right,  $\text{SNR} = 1.47 \times 10^2$ ). The black lines are the Schwarzschild limit of  $|f_I|/f_R \approx 0.236$ . The colored ellipses show the contours of  $1\sigma$ ,  $2\sigma$ ,  $3\sigma$ ,  $4\sigma$ , and  $5\sigma$ . To obtain these two dimensional plots, the time and phase parameters  $(t_0, \phi_0)$  have been marginalized out.

#### 4.3. A physical interpretation of quasinormal modes

According to Refs. [106,107], QNMs in GR arise as perturbations of stellar or BH spacetimes. In BBH mergers, the remnant objects are expected to be BHs in GR. When we confirm the BH QNMs in GW observations, what we can say is suggested in the following. The executive summary of this suggestion is that we may confirm the strong-field gravity based on Einstein’s GR within the ergosphere, when the QNM GW signals with  $a/M \gtrsim 0.7$  are observed by GW observatories with sufficient accuracy. The remnant BH of GW190521 has the spin  $a/M = 0.72^{+0.09}_{-0.12}$  [3], and we have shown in Section 3.3 and Section 4.2 that ET observation of the QNM frequency will be percent-level precision. The future observation GW190521-like BBH would thus provide a unique opportunity to access the salient strong-field feature of the Kerr BH.

The BH QNMs are calculated in the BH perturbation approach. The background spacetime is a Kerr BH [108] which is written in the Boyer–Lindquist coordinates  $(t, r, \theta, \phi)$  as

$$ds^2 = - \left(1 - \frac{2Mr}{\Sigma}\right) dt^2 - \frac{4Mar \sin^2 \theta}{\Sigma} dt d\phi + \frac{\Sigma}{\Delta} dr^2 + \Sigma d\theta^2 + \left(r^2 + a^2 + \frac{2Ma^2 r}{\Sigma} \sin^2 \theta\right) \sin^2 \theta d\phi^2, \quad (30)$$

where  $\Sigma = r^2 + a^2 \cos^2 \theta$ ,  $\Delta = r^2 - 2Mr + a^2$ , and  $M$  and  $a$  denote the mass and Kerr spin parameter, respectively (note the relation  $S = Ma = M^2 \chi$  for the spin). In this work, we employ the “Sasaki–Nakamura” formalism to deal with the gravitational perturbations [109–111], in which the radial homogeneous equation is formally written as (throughout in this section we ignore the label of  $(\ell, m, \omega)$  to improve the readability)

$$\frac{d^2 Y}{dr^{*2}} + (\omega^2 - V_{\text{SN}}) Y = 0, \quad (31)$$

with the tortoise coordinate  $r^*$  defined by  $dr^*/dr = (r^2 + a^2)/\Delta$ . The relation between the Teukolsky radial function  $R_{\ell m \omega}$  [112] and the Sasaki–Nakamura radial function  $Y$  (and also between the Teukolsky radial potential  $V_{\ell m \omega}$  and Sasaki–Nakamura radial potential  $V_{\text{SN}}$ ) is determined by two free functions  $g$  and  $h$  (see, for example, Ref. [113]). Their explicit expressions are summarized in Refs. [110,114], for both homogeneous and inhomogeneous equations.

There are various approaches to calculate the QNMs in literature (for example, Ref. [115]). The exact QNMs are obtained only numerically from, for example, the continued fraction method (known as Leaver’s method) [116]. In this subsection, alternatively, we consider the analytical WKB approximation of QNM [117–121] (see also Ref. [122] and references therein) to see an approximate (space) location where the QNMs would be generated, bearing in mind some ambiguity of the inferred location [123] as well as the limitation of the WKB (and other) approximation itself [124] (see also Refs. [125,126]).

In the WKB approach, the peak location of the potential can be considered as the location around which the QNMs are generated. Here, the word “around” has two meaning: i) the GW cannot be localized due to the equivalence principle, and ii) the imaginary part of the QNMs is determined by the curvature of the radial potential such as  $V_{\text{SN}}$  Eq. (31). The radial potential  $V_{\text{SN}}$  is complex in general, and the peak location is obtained in the complex plane. By good fortune, the Sasaki–Nakamura formalism involves the two free functions to relate to the Teukolsky equation, and one can make use of this freedom to have a simple radial potential so that it gives rise to a single strong peak around the real axis, specifying the responsible (real) radius where QNMs could be excited.

In practice, we estimate the peak radius  $r_0^*$  of the radial potential  $|V_{\text{SN}}|$  with a numerically given exact QNM frequency, by solving Eq. (31), in practice, in terms of  $r = r_0$ . And then, in the WKB approximation, the fundamental ( $n = 0$ ) QNM frequency is calculated by

$$(\omega_{\text{R}}^{\text{WKB}} + i\omega_{\text{I}}^{\text{WKB}})^2 = V_{\text{SN}}(r_0^*) - i\sqrt{-\frac{1}{2} \frac{d^2 V_{\text{SN}}}{dr^{*2}} \Big|_{r^*=r_0^*}}, \quad (32)$$

where  $\omega_{\text{R}}^{\text{WKB}}$  and  $\omega_{\text{I}}^{\text{WKB}}$  are the real and imaginary parts of the WKB QNM frequency, and  $V_{\text{SN}}$  in the right hand side of Eq. (32) is evaluated in terms of the exact values of QNM frequency. To gauge whether the approximation and evaluation of the peak location are reasonable or not, we check the frequency error,

$$\delta_{\text{R}} = \left| 1 - \frac{\omega_{\text{R}}^{\text{WKB}}}{\omega_{\text{R}}} \right|, \quad \delta_{\text{I}} = \left| 1 - \frac{\omega_{\text{I}}^{\text{WKB}}}{\omega_{\text{I}}} \right|, \quad (33)$$

where  $\omega_{\text{R}} = 2\pi f_{\text{R}}$  and  $\omega_{\text{I}} = 2\pi f_{\text{I}}$  are the real and imaginary parts of the accurate QNM frequency.

Let’s consider the simple Schwarzschild ( $a = 0$ ) case first in order to see the dependence of the WKB QNM frequencies on the choice of the potential. In this case, the gravitational perturbations is classified into the odd and even sector (in terms of  $(\ell, m)$  modes), and the radial homogeneous equations of each sectors have the Regge–Wheeler [127] and Zerilli [128] potentials, respectively. It is known that the same QNMs are derived from the two potentials which are related by the Chandrasekhar transformation [129]. The exact value of fundamental ( $\ell = 2, m = 2, n = 0$ ) QNM frequency is [71]

$$\omega_{\text{R}} \approx \frac{0.3736}{M}, \quad \omega_{\text{I}} \approx -\frac{0.08896}{M}. \quad (34)$$

To calculate the QNM frequency in the WKB approximation, we use the two potential. The peak radius of the Regge–Wheeler potential is

$$r_0^{\text{RW}} \approx 3.281M, \quad (35)$$

and that of the Zerilli potential becomes

$$r_0^Z \approx 3.099M. \quad (36)$$

The WKB QNM frequency is derived from Eq. (32) as

$$\omega_R^{\text{WKB}} \approx \frac{0.3988}{M}, \quad \omega_I^{\text{WKB}} \approx -\frac{0.08829}{M}, \quad (37)$$

for the Regge–Wheeler potential, and

$$\omega_R^{\text{WKB}} \approx \frac{0.3989}{M}, \quad \omega_I^{\text{WKB}} \approx -\frac{0.08835}{M}, \quad (38)$$

for the Zerilli potential. We see the difference in the above two frequencies. Using Eq. (33), the frequency errors become  $\delta_R^{\text{RW}} = 6.738\%$ ,  $\delta_I^{\text{RW}} = 0.7609\%$ ,  $\delta_R^Z = 6.750\%$ , and  $\delta_I^Z = 0.6871\%$ . We do not mention which potential is better and which peak location is better to describe the generation of the QNM from the small differences in the frequency errors. “Around”  $3M$  where the QNM is generated, will be the appropriate expression. In the large  $\ell$  limit, both of the potential have the peak location  $r = 3M$  which is the light ring radius (see Ref. [130] and references therein).

We proceed to the Kerr case. For example, we set the two free functions given in Ref. [113] as <sup>16</sup>

$$g = \frac{r(r-a)}{(r+a)^2}, \quad h = 1, \quad (40)$$

and calculate the peak radius  $r_0^*$  as well as the QNM frequencies in the WKB approximation (32). Although Ref. [113] applied the above choice of two free functions only to the potential  $V_{\text{SN}}$  with the Kerr spin  $0.98 \leq a/M < 1$  in , we find the associated  $V_{\text{SN}}$  always gives a peak radius as a smooth, monotonically decreasing function of the peak radius with respect to  $a/M$  beyond  $a/M = 0.98$ . Therefore, we use it for the full range of Kerr spins  $0 \leq a/M < 1$  here.

Figure 3 shows the peak location of the potential for the fundamental ( $n = 0, \ell = 2, m = 2$ ) mode as a function of the remnant spin  $0 \leq a/M < 1$ . We also present three radii: the outer horizon radius,

$$\frac{r_+}{M} = 1 + \sqrt{1 - \left(\frac{a}{M}\right)^2}, \quad (41)$$

the inner light ring radius [133],

$$\frac{r_{\text{lr}}}{M} = 2 + 2 \cos \left[ \frac{2}{3} \cos^{-1} \left( -\frac{a}{M} \right) \right], \quad (42)$$

---

<sup>16</sup> References [109,110] used a different choices of two free functions  $g$  and  $h$  given by

$$g = \frac{r^2 + a^2}{r^2}, \quad h = 1. \quad (39)$$

Historically, they are chosen so that the Sasaki–Nakamura potential  $V_{\text{SN}}$  becomes short range ( $\sim O(1/r^2)$ ), and the source term of the Sasaki–Nakamura formalism falls off like  $O(r^{-5/2})$  at infinity, and  $O(r - r_+)$  at the horizon [131]. However, Ref. [113] pointed out that the choice in Eq. (39) is not necessary unique to satisfy those conditions. In fact, the asymptotic forms of  $g$  and  $h$  only have to be  $g = O(r^0)$  and  $h = O(r^0)$  for  $r^* \rightarrow -\infty$  and  $g = O(r^0) + O(r^{-2})$  and  $h = O(r^0) + O(r^{-2})$  for  $r^* \rightarrow +\infty$ . One can see that both choices of Eqs. (39) and (40) respect this requirement, but the choice in Eq. (40) is particularly suitable for the WKB analysis to have a strong peak of the potential  $V_{\text{SN}}$  near the real axis; we refer the reader to, for example, Figure 1 of Ref. [132] to see the problematic behavior of  $V_{\text{SN}}$  near the peak with the original choice of Eq. (39).



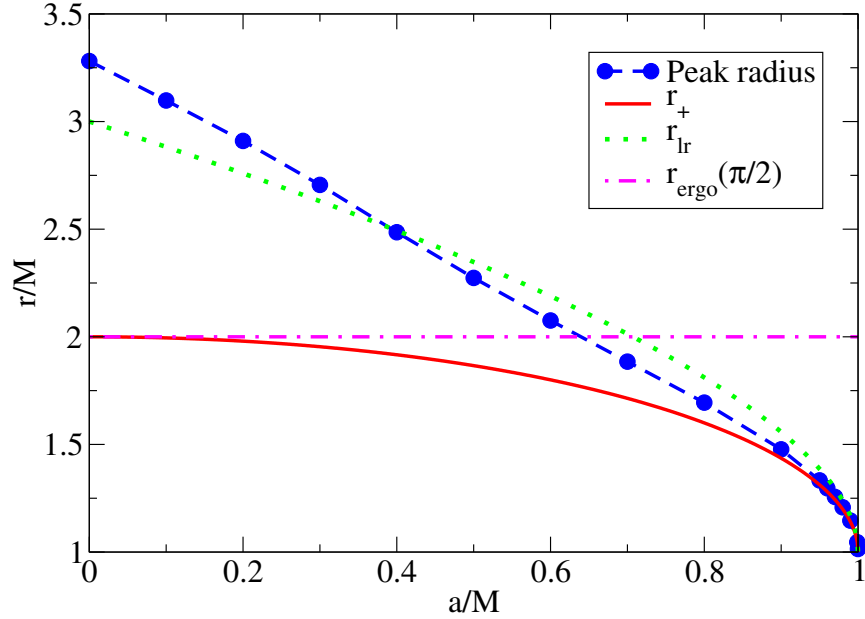


**Figure 3.** Estimation of “approximate” radius  $r_0$  where the fundamental ( $n = 0, \ell = 2, m = 2$ ) QNM may be excited. The outer horizon radius  $r_+$ , the inner light ring radius  $r_{lr}$ , and the equatorial radius of the ergosphere  $r_{\text{ergo}}(\theta = \pi/2)$  are also plotted.

and the radius of the ergosphere,

$$\frac{r_{\text{ergo}}(\theta)}{M} = 1 + \sqrt{1 - \left(\frac{a}{M}\right)^2 \cos^2 \theta}, \quad (43)$$

where the equatorial one is  $r_{\text{ergo}}(\theta = \pi/2)/M = 2$ . We see that the peak radius is below the equatorial radius of the ergosphere  $r_{\text{ergo}}(\theta = \pi/2)$  if the BH spin is  $a/M \gtrsim 0.7$ , which implies that the QNM may be excited *within* the ergoregion of the highly spinning Kerr BH.

We should, however, be careful of this estimation of the peak radius. Figure 4 shows the estimation of frequency errors between the accurate (true) QNM frequency,  $\omega_R + i\omega_I$ , and that obtained in the WKB approximation,  $\omega_R^{\text{WKB}} + i\omega_I^{\text{WKB}}$  as a consistency check. We have large errors ( $\gtrsim 10\%$ ) for the imaginary part of the QNM frequency when  $0.8 \lesssim a/M \lesssim 0.95$ . This means that the choice of the two free functions in Eq. (40) is not most appropriate to have a well-behaved potential in the WKB approximation for this range of  $a/M$ <sup>17</sup>.

## 5. Summary and Discussion

This work underlines the multiband observation of the GW190521-like nonprecessing, quasicircular “intermediate-mass” BBH with LISA and B-DECIGO in the low-frequency band, combined it with aLIGO and ET in the high-frequency band. Our first result of the parameter estimation errors was displayed in Tables 2 and 3; the statistical errors of the binary’s mass parameters by B-DECIGO observation will

<sup>17</sup> Nevertheless, we speculate that the position of the peak radii may not sensitively depend on the choice of the potential as far as the target potential has a single strong peak around the real axis. For example, we have used the different Detweiler potential [134] for  $0.7 \leq a/M < 0.97$  in Ref. [88], and we obtained the peak location within  $\sim 2\%$  frequency errors of our results here; in the case of  $a/M = 0.8$ , we have  $r_0 = 1.759M$  for the Detweiler potential and  $r_0 = 1.694M$  for our Sasaki–Nakamura potential. We do not, however, speculate any further.

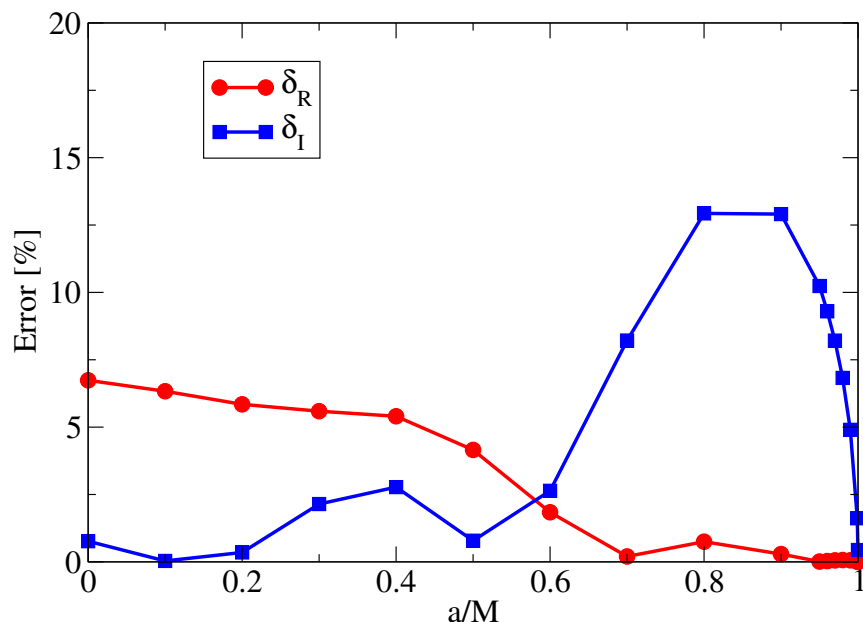


**Figure 4.** Errors in the real and imaginary parts of the QNM frequency in the WKB approximation,  $\delta_R = |1 - \omega_R^{\text{WKB}}/\omega_R|$  and  $\delta_I = |1 - \omega_I^{\text{WKB}}/\omega_I|$  with the accurate QNM frequency  $\omega_R + i\omega_I$  and the WKB QNM frequency  $\omega_R^{\text{WKB}} + i\omega_I^{\text{WKB}}$ , respectively.

be  $\sim 10^{-2}$ , and the multiband LISA, B-DECIGO and ET will further improve them to a factor of 2, even allowing the statistical errors of component BH spins at the accuracy level of  $\sim 10^{-1}$ . Based on the ringdown analysis, ET will measure the QNM frequency about  $O(0.1)\%$  precision. Our second result of GR tests was presented in Table 4 as well as Figures. 2 and 3. We showed that the multiband observation of GW190521-like BBH system by LISA, B-DECIGO and ET would perform the inspiral–(merger)–ringdown consistency test at the level of percent-precision. We also argued that the accurate QNM frequency measured by ET would be able to verify the remnant compact object to be a Kerr BH predicted by GR, proving its ergoregion.

The main point of our analysis is that there is the principal advantage of measuring GW190521-like BBH systems using *the full GW spectrum* from milli-Hz to deci-Hz band, and to hecto-Hz band. We expect our findings will motivate further investigation on prospects for multiband observation of GW190521-like BBH systems, in addition to the prototypical GW150914-like BBH system [22].

Nevertheless, we emphasize that our study were performed with (very) simple methods. Therefore, our results should be only *indicative* and *tentative*. In the remainder of this section, we discuss what works remain to be done to refine our analysis in future, so that we can eventually make a strong scientific cases of multiband GW astronomy/physics.

### 5.1. Assessment of prospects

First, our methodology in Section 2 should be replaced with more modern, sophisticated approaches to the GW data analysis; it will include (but not limited to), for example, the use of complete IMR waveforms such as “effective-one-body” (EOB) approach as well as “phenomenological” (IMRPhenom) models (see, for examples, Ref. [135] and references therein), full-fledged Bayesian posterior based techniques (see, for examples, Refs. [101,136,137]), and more ‘realistic’ noise and waveform models that account for the sky-location of sources as well as orbital configurations of B-DECIGO [11] and LISA [8].

Second, our target GW190521-like BBH system was restricted to the nonprecessing, spinning, quasicircular configuration; although there is large uncertainty, the spin precession of GW190521 is estimated as nonzero [3,4]. Future studies are therefore needed to concern both the spin precession and orbital eccentricity of the BBH system: we will briefly discuss the eccentric, non-spinning BBH system in Appendix A. In general, the BH's spins in the precessing binary have not only their magnitudes but also orientations, which can be described by, for examples, the effective inspiral spin parameter  $\chi_{\text{eff}}$  (related to the components aligned with the orbital angular momentum), and the precession spin parameter  $\chi_p$  (related to the components in the orbital plane for the inspiral GW waveform). Adding the orbital eccentricity to the (precessing) BBH system will be fully generic, and the waveform modeling becomes (much) more complicated. Despite that challenge, there is a considerable development of the analysis on fully generic binary systems [138].

Related with the point mentioned above, it should be noted that we have ignored subdominant ( $\ell \neq 2$ ,  $|m| \neq 2$ ) harmonics in our GW waveform model. They are more notable in the observed signal when system's mass ratio becomes smaller (such as the analysis of GW190814 [139] with mass ratio  $q = 0.112_{-0.009}^{+0.008}$ ). With the subdominant harmonics, one can access the source orientation to reduce uncertainty in the distance estimation [140].

Third, we should note that there are two main hurdles to analyze the ringdown GW signals; the low SNR with aLIGO, and the starting time of the ringdown phase that is *a priori* unknown to the whole observed GW signal (see, for examples, Refs. [141,142] for discussions on the starting time). Our simple analysis is carried out with the single-mode waveform model (11) as the template to analyse the ringdown phase, assuming that the starting time of the ringdown phase to be  $t = t_0$  which corresponds to the  $f = f_R$ , i.e., just after the end of the merger phase. While this choice does not affect our results of parameter estimation errors, in practice, the best fit values (that should be obtained rather than assumed in the context of the full parameter estimation against the raw GW data) can be biased if one assumes the earlier starting time in the analysis (see, for example, Figure 5 in Ref. [84]). Although one may delay the starting time to avoid the bias in the parameter estimation, the SNR becomes much lower than the expected SNR with the assumption of  $t = t_0$ .

These obstacles will be overcome if one includes higher overtones ( $n > 0$ ) into the ringdown GW analysis [143], for which a much larger SNR than the single-mode analysis will be expected. Indeed, a superposition of overtones ( $n > 0$ ) in a single harmonic mode will be observed [143–146] in the high SNR events (with ET). Another step-functional improvement of the ringdown GW analysis will be offered by using completely different signal-analysis methods than the traditional matched filtering analysis, which may not be always optimal for the ringdown GW signal. There is ongoing work to assess the improvement due to new techniques for the ringdown GW signal analysis (such as Hilbert–Huang transformation, autoregressive modeling, and neural network) [147,148].

Fourth, there are other types of GR test that were not covered in Section 4, but can be greatly improved using the multiband observation of GW190521-like BBH systems. Reference [87] performs various tests of GR with the BBH events in GWTC-2 (see also the reviews by Carson and Yagi [149] about the current and future test with GWs), including i) the IMR consistency test between the inspiral and postinspiral phases divided at some cutoff frequency; ii) constraining deviations from GR with parametric deformations to a predicted GR waveform model, iii) “BH spectroscopy” [150,151] with ringdown GWs which contains two (or possibly more) QNMs [152,153], and so on.

The test i) is similar to our “inspiral–ringdown test” directly using the information of the merger phase, and makes the most of the GW waveform. It has been pointed out that the values of this test with GW150914-like BBH systems will be maximized in the multiband observation [28,29,154]. Our result suggests that the same will be true for the GW190521-like “intermediate-mass” BBH system, too. Similarly, Gupta et al. [31,32] have showed that the multiband observations of stellar- and intermediate-mass BBHs

with LISA and 3G detectors will be only workable way to carry out the most general version of test ii). Adding B-DECIGO (or any other planned GW detectors) in the deci-Hz band to the multiband analysis, we expect the precision of this test will be unprecedented.

Based on the generalized likelihood ratio test [155], the test iii) is performed (see, for examples, Section 9.5 in Ref. [156] and references therein, and also Ref. [157] for the future O5 era). This test with aLIGO and Advanced Virgo alone is quite challenging to have any conclusive result, simply because of the too low SNRs and the larger parameter estimation errors in the ringdown phase. In the 3G era, two (or possibly more) QNMs will be measurable [152,153]. It is also helpful to use the multiband observation in order to optimize ground-based detectors via the forewarnings from the low-frequency, LISA band [158]. In either cases, multibanding with B-DECIGO and ET will give them additional advantage of being able to perform the best test of Kerr hypothesis of remnant BHs via BH spectroscopy.

**Author Contributions:** The authors contribute equally to this paper.

**Funding:** H. N. acknowledges support from JSPS KAKENHI Grant No. JP16K05347. S. I. acknowledges support from STFC through Grant No. ST/R00045X/1. S. I. also thanks to networking support by the GWverse COST Action CA16104, "Black holes, gravitational waves and fundamental physics." N. S. and H. N. acknowledge support from JSPS KAKENHI Grant No. JP17H06358.

**Acknowledgments:** We would like to thank Carlos O. Lousto, James Healy and Leor Barack for useful discussion. All the analytical and numerical calculations in this paper have been performed with *Maple* and Black Hole Perturbation Club (B.H.P.C.) codes [71].

**Conflicts of Interest:** The authors declare no conflict of interest.

## Appendix A. Signal-to-noise ratio of GW190521-like eccentric BBH systems

Throughout the bulk of this paper, we have looked at GW190521-like BBH systems under the assumption of a quasicircular BBH merger. While the quasicircular evolution of GW190521 is totally consistent with the LIGO/Virgo observation [3,4], due to the lack of the inspiral GW signal long enough, it appears that alternative scenarios, for example, GW190521 as an eccentric BBH merger also becomes relevant. Indeed, Gayathri et al. [44] demonstrated that observed GW190521 data could be explained as an equal-mass, highly-eccentric ( $e = 0.7$ ) BBH system<sup>18</sup>, and the estimated source parameters are quite different from those derived from the quasicircular BBH scenario (recall Table 1): the primary mass  $m_1^r = 102_{-11}^{+7} M_\odot$ , the secondary mass  $m_2^r = 102_{-11}^{+7} M_\odot$ , and the total mass  $m_t^r = 204_{-33}^{+14} M_\odot$  in the source's rest frame, the mass ratio  $q = 1$ , the luminosity distance  $D_L = 1.84_{-0.054}^{+1.07}$  Gpc and the redshift  $z = 0.35_{-0.09}^{+0.16}$  (see Ref. [44] for the spin parameters). The possibility of GW190521 with nonvanishing eccentricity is also pointed out by Refs. [160,161].

Like the quasicircular case, the multiband observation of eccentric GW190521-like BBH systems will once again help in distinguishing these two scenarios. Assuming a quadrupole GW generation from a Newtonian Kepler orbit [162,163], the typical coalescing time  $t_c^{\text{ecc}}$  and the characteristic strain amplitude  $h_{c,n}^{\text{ecc}}$  of the  $n$ -th harmonic are (see, for example, Section 4.1 of Maggiore's text [164] as well as Ref. [165])

$$t_c^{\text{ecc}} \sim t_c^{\text{circ}} (1 - e_0^2)^{7/2}, \quad h_{c,n}^{\text{ecc}} \sim h_{c,n}^{\text{circ}} g(n, e), \quad (\text{A1})$$

where  $t_c^{\text{circ}}$  and  $h_{c,n}^{\text{circ}}$  are corresponding circular-inspiral results given in Eqs. (1) and (3), respectively, and the function  $g(n, e)$  will be defined momentarily. We see that the early inspiral phase of the eccentric

---

<sup>18</sup> The orbital eccentricity ( $e = 0.7$ ) is provided as initial data for NR simulations at a frequency of 10 Hz for a system with the total mass of  $50 M_\odot$  that is the orbital separation  $\sim 24.5 m_t$  for BBHs with the total mass  $m_t$  [159]. The NR waveforms are scaled by the total mass  $m_t$ .

binary is well within the B-DECIGO and LISA bands, too. Specifically, Holgado et al. [166] (see also the series of work by Amaro-Saoane [42,165,167]) pointed out that having deci-Hz GW observatories such as B-DECIGO, MAGIS [14] and TianGO [15] will be a key element to observe the eccentric inspiral GW signals in the multiband because the GW signal may skip the LISA band entirely;  $h_{c,n}^{\text{ecc}}$  can be suppressed by a function of  $g(n, e)$  significantly, depending on its eccentricity in the LISA band.

To better understand the visibility of eccentric BBH systems with aLIGO, ET, B-DECIGO and LISA, let us estimate the SNR of non-spinning, eccentric BBH inspirals accumulated in each band; see also Ref. [168] for a recent review about waveform families for the eccentric binary systems. The squared SNR averaged over the all-sky positions and binary orientations may be written as [23,51,78,169]<sup>19</sup>

$$\rho_{\text{ave}}^2 \approx \frac{1}{5} \sum_n \int_{f_{\text{in}}}^{f_{\text{end}}} \frac{h_{c,n}^2}{f_n S(f)} d(\ln f_n), \quad (\text{A2})$$

where  $S(f)$  is the noise PSD for a given GW detector, and

$$f_n = n f_{\text{orb}} = n f_{\text{orb}}^r (1+z)^{-1}, \quad (\text{A3})$$

is the frequency of the harmonic in the observer frame, defined by the source's rest-frame frequency  $f_{\text{orb}}^r$  of the Kepler orbit with the redshift  $z$ . The dimensionless characteristic strain  $h_{c,n}$  of the  $n$ -th harmonic is [169]

$$h_{c,n} \equiv \frac{1+z}{\pi D_L} \sqrt{2 \frac{dE_n^r}{df_n^r}}, \quad (\text{A4})$$

where  $D_L$  is the luminosity distance. Assuming the quadrupole formula applied to the Kepler orbit (with the chirp mass  $\mathcal{M}$  in the observer frame) [162,163],

$$\frac{dE_n^r}{df_n^r} \equiv \frac{\pi}{3} \frac{\mathcal{M}^{5/3}}{(1+z)^2} \frac{g(n, e)}{F(e)} \left(\frac{2}{n}\right)^{2/3} (\pi f_n)^{-1/3}, \quad (\text{A5})$$

is the emitted GW energy per unit frequency  $f_n^r$  at the  $n$ -th harmonic measured in the source's rest frame, and we define

$$g(n, e) \equiv \frac{n^4}{32} \left\{ \left[ J_{n-2}(ne) - 2e J_{n-1}(ne) + \frac{2}{n} J_n(ne) + 2e J_{n+1}(ne) - J_{n+2}(ne) \right]^2 \right. \\ \left. + (1-e^2) [J_{n-2}(ne) - 2J_n(ne) + J_{n+2}(ne)]^2 + \frac{4}{3n^2} J_n^2(ne) \right\}, \quad (\text{A6})$$

$$F(e) \equiv \frac{1 + \frac{73}{24} e^2 + \frac{37}{96} e^4}{(1-e^2)^{7/2}} \left( = \sum_{n=1}^{\infty} g(n, e) \right), \quad (\text{A7})$$

with the Bessel functions of the first kind  $J_n(x)$  ( $n$ : integer); see, for example, Ref. [170] for the derivation of Eq. (A5).

<sup>19</sup> The expression for the average SNR (A2) recovers Eq. (17) (of the inspiral part) in the circular orbit limit,  $e \rightarrow 0$ . Note that the harmonics are restricted to only  $n = 2$  in the circular limit because one has  $\lim_{e \rightarrow 0} g(n, e) = \delta_{2,n}$ .

For an inspiraling eccentric BBH, the evaluation of SNR through Eq. (A2) requires the knowledge of slowly-evolving orbital eccentricity  $e$  and the frequency  $f_n$  in time, under the gravitational radiation losses. Again, in the quadrupole formalism, it is given by [162,163]

$$\frac{f_{\text{orb}}}{f_{\text{orb},0}} = \left[ \frac{1 - e_0^2}{1 - e^2} \left( \frac{e}{e_0} \right)^{12/19} \left( \frac{1 + \frac{121}{304} e^2}{1 + \frac{121}{304} e_0^2} \right)^{870/2299} \right]^{-3/2}, \quad (\text{A8})$$

with reference eccentricity  $e_0$  and orbital frequency  $f_{\text{orb},0}$  (in the observer frame). One can set these constants by the values at the last stable orbit of the eccentric geodesic (of a test particle) in the Schwarzschild geometry [171]: namely,  $e_0 = e_{\text{LSO}}$  and

$$\begin{aligned} f_{\text{orb},0} = f_{\text{LSO}} &= \frac{1}{2\pi(1+z)m_t^r} \left( \frac{1 - e_{\text{LSO}}^2}{6 + 2e_{\text{LSO}}} \right)^{3/2} \\ &\sim 8.0 (1+z)^{-1} \left( \frac{m_t^r}{204M_\odot} \right)^{-1} \left( \frac{1 - e_{\text{LSO}}^2}{6 + 2e_{\text{LSO}}} \right)^{3/2} \text{ Hz}, \end{aligned} \quad (\text{A9})$$

with the total mass  $m_t^r$  in the source's rest frame. The frequency evolution (A8) is therefore completely determined with a given single parameter  $e_{\text{LSO}}$ .

We compute the averaged SNR  $\rho_{\text{ave}}$  given in Eq. (A2) for the GW190521-like, non-spinning, eccentric BBHs with the source-frame masses  $(m_1^r, m_2^r) = (102 M_\odot, 102 M_\odot)$  and the luminosity distance  $D_L = 1.9 \text{ Gpc}$  (i.e., the redshift  $z \sim 0.35$ ), which mimics the eccentric BBH merger obtained by the NR simulations in Ref. [44]. We assume the five year observation prior to the final merger determined by Eqs. (A1) and (A9), and apply the same setup described in Section 3.1 to each  $n$ -th harmonic of GW strains. Because the frequency evolution (A8) is expressed in term of eccentricity, in practice, we change the integration variable of Eq. (A2) from  $f_n$  to  $e$  for the computational efficiency, making use of  $df_n = n|df_{\text{orb}}/de|de$  with (see, for example, Ref. [172])

$$\frac{df_{\text{orb}}}{de} = -\frac{18}{19} \frac{f_{\text{orb}}}{e} \frac{F(e)}{(1 - e^2)^{9/2} \left( 1 + \frac{121}{304} e^2 \right)}. \quad (\text{A10})$$

Also, the infinite summation over the harmonics  $n$  in Eq. (A2) are truncated at some finite value of  $n_{\text{max}}$ ; we chose  $n_{\text{max}} = O(10^4)$  so that the resultant SNRs are guaranteed to have at least 3 significant digits<sup>20</sup>.

In Table A1, we summarize the averaged SNRs  $\rho_{\text{ave}}$  of GW190521-like, non-spinning, eccentric BBHs accumulated in each GW band, for sample values of final eccentricities at the last stable orbit  $e_{\text{LSO}} = \{10^{-6}, 10^{-3}, 0.1, 0.4, 0.6\}$ . For references, the 'initial' eccentricities at  $f_{\text{in}}$  for each band are also listed. It is approximated by solving Eq. (A8) for  $e$  at the detector's initial GW frequency of the second harmonics  $f_{\text{orb}} = f_{\text{in}}/2$ . We found three main results: i) B-DECIGO and ET always have the SNR larger than at least 10 independent of the values of final eccentricity  $e_{\text{LSO}}$ ; ii) LISA has the detectable SNR only when  $e_{\text{LSO}} < 10^{-3}$ . That is, the inspiral GW signal from GW190521-like BBH that has a high-eccentricity in the aLIGO band would entirely skip the LISA band; iii) The SNR with B-DECIGO becomes bigger when  $e_{\text{LSO}}$  becomes smaller, while the SNR with ET and aLIGO shows the opposite behavior. Therefore, the mutibanding could provide much louder SNR than the single-band SNR across the full range of  $e_{\text{LSO}}$ .

<sup>20</sup> A good analytical estimator of  $n_{\text{max}}$  can be found in, for examples, Refs. [173,174].

Using Eq. (21) with the result in Table A1, we find that the multiband SNR with B-DECIGO and ET are  $\sim 180$  for  $e_{\text{LSO}} = \{10^{-6}, 10^{-3}\}$ ,  $\sim 140$  for  $e_{\text{LSO}} = \{0.4, 0.6\}$  and  $\sim 100$  for  $e_{\text{LSO}} = 0.1$ .

**Table A1.** Averaged SNRs  $\rho_{\text{ave}}$  of the GW190521-like, non-spinning, eccentric BBHs accumulated in each band five years prior to coalescence, for a given values of final eccentricity  $e = e_{\text{LSO}}$ . We assume the source-frame component masses  $(m_1^r, m_2^r) = (102 M_\odot, 102 M_\odot)$ , and the luminosity distance  $D_L = 1.9 \text{ Gpc}$  (i.e., the redshift  $z \sim 0.35$ ) [44]. The values in parentheses indicate the ‘initial’ eccentricity estimated from the initial GW frequency ( $f_{\text{in}}$  defined in Section 3) of the second harmonics in each detectors. Note that aLIGO’s ‘initial’ eccentricity when  $e_{\text{LSO}} = 0.6$  is not displayed because the second harmonics is not detectable in this case.

	SNR and eccentricity at $f_{\text{in}}$				
	$e_{\text{LSO}} = 10^{-6}$	$e_{\text{LSO}} = 10^{-3}$	$e_{\text{LSO}} = 0.1$	$e_{\text{LSO}} = 0.4$	$e_{\text{LSO}} = 0.6$
aLIGO	4.95 ( $1.64 \times 10^{-6}$ )	4.95 ( $1.64 \times 10^{-3}$ )	5.55 (0.150)	$1.07 \times 10^1$ (0.405)	$1.11 \times 10^1$ ( $\dots$ )
ET	$7.64 \times 10^1$ ( $8.98 \times 10^{-6}$ )	$7.63 \times 10^1$ ( $8.97 \times 10^{-3}$ )	$8.73 \times 10^1$ (0.505)	$1.42 \times 10^2$ (0.746)	$1.42 \times 10^2$ (0.793)
B-DECIGO	$1.67 \times 10^2$ ( $2.41 \times 10^{-3}$ )	$1.70 \times 10^2$ (0.709)	$5.08 \times 10^1$ (0.982)	$1.85 \times 10^1$ (0.992)	$1.20 \times 10^1$ (0.993)
LISA	7.60 ( $3.86 \times 10^{-3}$ )	2.05 (0.985)	$< 1.00$ ( $> 0.999$ )	$< 1.00$ ( $> 0.999$ )	$< 1.00$ ( $> 0.999$ )

Finally, although the parameter estimation is not the main focus here, we briefly discuss the potential accuracy of the eccentricity measurement. In the small-eccentricity and high-SNR limit, the orbital eccentricity may be measured within the fractional errors [175] (see also Ref. [176])

$$\delta \hat{e}_0 \sim 5 \times 10^{-5} \frac{(1+z)^{5/3}}{\sqrt{2+3\alpha}} \left( \frac{\mathcal{M}^r}{65.1 M_\odot} \right)^{5/3} \left( \frac{f_0}{0.1 \text{ Hz}} \right)^{5/3} \left( \frac{e_0}{0.1} \right)^{-1}, \quad (\text{A11})$$

from Eq. (2) in Ref. [175] by using a rough approximation with the quasicircular amplitude and the eccentric phase, where  $\delta \hat{e}_0$  denotes the parameter estimation error of  $e_0$  (at the GW frequency  $f_0$  for  $n = 2$ ) normalized by the SNR. Here, the power  $\alpha$  is due to the approximation noise PSD by a power law,  $S_n \sim f^{2\alpha}$  (assuming  $\alpha > -2/3$ ), and B-DECIGO may have  $\alpha = 1$ , for example. This estimator implies that B-DECIGO would be able to precisely measure the eccentricity of GW190521-like BBH systems. Because we find that the ‘B-DECIGO + ET’ combination always provides the multiband SNRs larger than  $\sim 100$  independent of the value of  $e_{\text{LSO}}$ , one might expect that this multibanding best observes GW190521-like BBHs over the full range of eccentricity, helping to understand the population properties of BBH mergers [177]. We will explore this possibility in future work.

## Appendix B. Some more noise power spectral densities of (next-generation) GW detectors

In this appendix, we summarize some (fitting) curves of the noise PSD of both ground and space-based, current and future GW detectors. These sensitivity curves are not used in the bulk of this paper, but it will serve as a convenient all-in-one-place summary with our notation; these curves with  $f/(1 \text{ Hz})$  are shown in Figure 4 of Ref. [178] (except DECIGO and TianQin).

- “LIGO O3a-Livingston” rough fitting curve (during the first half of LIGO/Virgo third observing run by using Ref. [179]):

$$S_n^{\text{O3a-L}} = \left( 2.13068 \times 10^{-12} f^{-7.938724592} + 4.0 \times 10^{-22} f^{-1.0} + 3.0 \times 10^{-24} + 1.74546 \times 10^{-27} f^{1.178746922} \right)^2 \text{ Hz}^{-1}. \quad (\text{A12})$$

- “LIGO O5” rough fitting curve (will be in the fifth observing run by using Ref. [179]):

$$S_n^{\text{O5}} = \left( 480985000.0 f^{-30.28419138} + 6.63263 \times 10^{-20} f^{-3.122716032} + 6.15101 \times 10^{-21} f^{-2.089976737} + 1.32853 \times 10^{-27} f^{1.059219544} \right)^2 \text{ Hz}^{-1}. \quad (\text{A13})$$

- “ET-B” (another sensitivity curve for ET in Ref. [180] other than Eq. (5); see also, for examples, Ref. [181] and ET sensitivity page [182]):

$$S_n^{\text{ET-B}} = 1.0 \times 10^{-50} \left( 45540.5 f^{-15.64} + 6804.96 f^{-2.145} + 3.05853 f^{-0.12} + 0.00258062 f^{1.1} \right)^2 \text{ Hz}^{-1}. \quad (\text{A14})$$

- “CE2” rough fitting curve (for Cosmic Explorer presented in Ref. [21]):

$$S_n^{\text{CE2}} = \left( 1.74408 \times 10^{-16} f^{-8.908164528} + 2.0 \times 10^{-25} + 8.23008 \times 10^{-32} f^{2.095903274} \right)^2 \text{ Hz}^{-1}. \quad (\text{A15})$$

- “DECIGO” (the noise PSD of the L-shaped configuration [183]):

$$S_n^{\text{DECIGO}} = \left\{ 7.05 \times 10^{-48} \left[ 1 + \left( \frac{f}{f_p} \right)^2 \right] + 4.8 \times 10^{-51} f^{-4} \left[ 1 + \left( \frac{f}{f_p} \right)^2 \right]^{-1} + 5.53 \times 10^{-52} f^{-4} \right\} \text{ Hz}^{-1}. \quad (\text{A16})$$

with  $f_p \equiv 7.36$ . Note that this expression accounted for the factor of  $(\sqrt{3}/2)^{-2}$  due to DECIGO having arms that make an angle of  $60^\circ$ .

- “TianQin” [13,184] (the sky averaged noise PSD; the expression below is quoted from Eqs. (9) and (10) of Ref. [185]):

$$S_n^{\text{TianQin}} = 3.0 \times 10^{-51} \left( 0.009505539123 f^{-5} + 95.05539123 f^{-4} + 0.07550033531 f^{-3} + 755.0033531 f^{-2} + 3.703703703 \times 10^{10} + 2.941767614 \times 10^{11} f^2 \right) \text{ Hz}^{-1}. \quad (\text{A17})$$

## References

1. B. P. Abbott *et al.* [LIGO Scientific and Virgo], Phys. Rev. X **9** (2019) no.3, 031040 [arXiv:1811.12907 [astro-ph.HE]].



2. R. Abbott *et al.* [LIGO Scientific and Virgo], [arXiv:2010.14527 [gr-qc]].
3. R. Abbott *et al.* [LIGO Scientific and Virgo], Phys. Rev. Lett. **125**, no.10, 101102 (2020) [arXiv:2009.01075 [gr-qc]].
4. R. Abbott *et al.* [LIGO Scientific and Virgo], Astrophys. J. Lett. **900**, no.1, L13 (2020) [arXiv:2009.01190 [astro-ph.HE]].
5. P. A. R. Ade *et al.* [Planck], Astron. Astrophys. **594** (2016), A13 [arXiv:1502.01589 [astro-ph.CO]].
6. V. Varma, S. E. Field, M. A. Scheel, J. Blackman, D. Gerosa, L. C. Stein, L. E. Kidder and H. P. Pfeiffer, Phys. Rev. Research. **1**, 033015 (2019) [arXiv:1905.09300 [gr-qc]].
7. A. H. Nitz and C. D. Capano, [arXiv:2010.12558 [astro-ph.HE]].
8. P. Amaro-Seoane *et al.*, arXiv:1702.00786 [astro-ph.IM].
9. T. Nakamura, M. Ando, T. Kinugawa, H. Nakano, K. Eda, S. Sato, M. Musha, T. Akutsu, T. Tanaka and N. Seto, *et al.* PTEP **2016**, no.9, 093E01 (2016) [arXiv:1607.00897 [astro-ph.HE]].
10. N. Seto, S. Kawamura and T. Nakamura, Phys. Rev. Lett. **87**, 221103 (2001) [astro-ph/0108011].
11. S. Kawamura, M. Ando, N. Seto, S. Sato, M. Musha, I. Kawano, J. Yokoyama, T. Tanaka, K. Ioka and T. Akutsu, *et al.* [arXiv:2006.13545 [gr-qc]].
12. W. H. Ruan, Z. K. Guo, R. G. Cai and Y. Z. Zhang, Int. J. Mod. Phys. A **35**, no.17, 2050075 (2020) [arXiv:1807.09495 [gr-qc]].
13. J. Luo *et al.* [TianQin], Class. Quant. Grav. **33**, no.3, 035010 (2016) [arXiv:1512.02076 [astro-ph.IM]].
14. P. W. Graham and S. Jung, Phys. Rev. D **97**, no.2, 024052 (2018) [arXiv:1710.03269 [gr-qc]].
15. K. A. Kuns, H. Yu, Y. Chen and R. X. Adhikari, Phys. Rev. D **102**, no.4, 043001 (2020) [arXiv:1908.06004 [gr-qc]].
16. W. T. Ni, Int. J. Mod. Phys. D **25** (2016) no.14, 1630001 [arXiv:1610.01148 [astro-ph.IM]].
17. W. T. Ni, Int. J. Mod. Phys. D **29** (2020) no.04, 1902005 [arXiv:2004.05590 [gr-qc]].
18. T. Akutsu *et al.* [KAGRA], [arXiv:2005.05574 [physics.ins-det]].
19. S. Hild, S. Chelkowski, A. Freise, J. Franc, N. Morgado, R. Flaminio and R. DeSalvo, Class. Quant. Grav. **27**, 015003 (2010) [arXiv:0906.2655 [gr-qc]].
20. M. Punturo *et al.*, Class. Quant. Grav. **27**, 194002 (2010).
21. D. Reitze, R. X. Adhikari, S. Ballmer, B. Barish, L. Barsotti, G. Billingsley, D. A. Brown, Y. Chen, D. Coyne and R. Eisenstein, *et al.* Bull. Am. Astron. Soc. **51**, 035 [arXiv:1907.04833 [astro-ph.IM]].
22. B. P. Abbott *et al.* [LIGO Scientific and Virgo], Phys. Rev. Lett. **116**, no.6, 061102 (2016) [arXiv:1602.03837 [gr-qc]].
23. A. Sesana, Phys. Rev. Lett. **116** (2016) no.23, 231102 [arXiv:1602.06951 [gr-qc]].
24. C. Cutler, E. Berti, K. Jani, E. D. Kovetz, L. Randall, S. Vitale, K. W. K. Wong, K. Holley-Bockelmann, S. L. Larson and T. Littenberg, *et al.* [arXiv:1903.04069 [astro-ph.HE]].
25. S. Vitale, Phys. Rev. Lett. **117** (2016) no.5, 051102 [arXiv:1605.01037 [gr-qc]].
26. K. Jani, D. Shoemaker and C. Cutler, Nature Astron. **4** (2019) no.3, 260-265 [arXiv:1908.04985 [gr-qc]].
27. E. Barausse, N. Yunes and K. Chamberlain, Phys. Rev. Lett. **116** (2016) no.24, 241104 [arXiv:1603.04075 [gr-qc]].
28. Z. Carson and K. Yagi, Class. Quant. Grav. **37** (2020) no.2, 02LT01 [arXiv:1905.13155 [gr-qc]].
29. Z. Carson and K. Yagi, Phys. Rev. D **101** (2020) no.4, 044047 [arXiv:1911.05258 [gr-qc]].
30. A. Toubiana, S. Marsat, S. Babak, E. Barausse and J. Baker, Phys. Rev. D **101** (2020) no.10, 104038 [arXiv:2004.03626 [gr-qc]].
31. A. Gupta, S. Datta, S. Kastha, S. Borhanian, K. G. Arun and B. S. Sathyaprakash, Phys. Rev. Lett. **125** (2020) no.20, 201101 [arXiv:2005.09607 [gr-qc]].
32. S. Datta, A. Gupta, S. Kastha, K. G. Arun and B. S. Sathyaprakash, [arXiv:2006.12137 [gr-qc]].
33. D. Gerosa, S. Ma, K. W. K. Wong, E. Berti, R. O'Shaughnessy, Y. Chen and K. Belczynski, Phys. Rev. D **99** (2019) no.10, 103004 [arXiv:1902.00021 [astro-ph.HE]].
34. K. K. Y. Ng, M. Isi, C. J. Haster and S. Vitale, Phys. Rev. D **102** (2020) no.8, 083020 [arXiv:2007.12793 [gr-qc]].
35. A. Toubiana, L. Sberna, A. Caputo, G. Cusin, S. Marsat, K. Jani, S. Babak, E. Barausse, C. Caprini and P. Pani, *et al.* [arXiv:2010.06056 [astro-ph.HE]].
36. B. Ewing, S. Sachdev, S. Borhanian and B. S. Sathyaprakash, [arXiv:2011.03036 [gr-qc]].
37. R. Nair, S. Jhingan and T. Tanaka, PTEP **2016** (2016) no.5, 053E01 [arXiv:1504.04108 [gr-qc]].
38. S. Isoyama, H. Nakano and T. Nakamura, PTEP **2018**, no.7, 073E01 (2018) [arXiv:1802.06977 [gr-qc]].

39. R. Nair and T. Tanaka, JCAP **08** (2018), 033 [erratum: JCAP **11** (2018), E01] [arXiv:1805.08070 [gr-qc]].
40. S. Grimm and J. Harms, Phys. Rev. D **102** (2020) no.2, 022007 [arXiv:2004.01434 [gr-qc]].
41. C. Liu, L. Shao, J. Zhao and Y. Gao, Mon. Not. Roy. Astron. Soc. **496** (2020) no.1, 182-196 [arXiv:2004.12096 [astro-ph.HE]].
42. P. Amaro-Seoane and L. Santamaria, Astrophys. J. **722** (2010), 1197-1206 [arXiv:0910.0254 [astro-ph.CO]].
43. K. Yagi, Class. Quant. Grav. **29** (2012), 075005 [arXiv:1202.3512 [astro-ph.CO]].
44. V. Gayathri, J. Healy, J. Lange, B. O'Brien, M. Szczepanczyk, I. Bartos, M. Campanelli, S. Klimentko, C. Lousto and R. O'Shaughnessy, [arXiv:2009.05461 [astro-ph.HE]].
45. P. Ajith, Phys. Rev. D **84**, 084037 (2011) [arXiv:1107.1267 [gr-qc]].
46. B. S. Sathyaprakash and B. F. Schutz, Living Rev. Rel. **12**, 2 (2009) [arXiv:0903.0338 [gr-qc]].
47. T. Robson, N. J. Cornish and C. Liu, Class. Quant. Grav. **36** (2019) no.10, 105011 [arXiv:1803.01944 [astro-ph.HE]].
48. A. Bohé, L. Shao, A. Taracchini, A. Buonanno, S. Babak, I. W. Harry, I. Hinder, S. Ossokine, M. Pürrer and V. Raymond, *et al.* Phys. Rev. D **95** (2017) no.4, 044028 [arXiv:1611.03703 [gr-qc]].
49. G. Pratten, S. Husa, C. Garcia-Quiros, M. Colleoni, A. Ramos-Buades, H. Estelles and R. Jaume, Phys. Rev. D **102** (2020) no.6, 064001 [arXiv:2001.11412 [gr-qc]].
50. E. Berti, A. Buonanno and C. M. Will, Phys. Rev. D **71**, 084025 (2005) [gr-qc/0411129].
51. N. Dalal, D. E. Holz, S. A. Hughes and B. Jain, Phys. Rev. D **74** (2006), 063006 [arXiv:astro-ph/0601275 [astro-ph]].
52. C. K. Mishra, A. Kela, K. G. Arun and G. Faye, Phys. Rev. D **93** (2016) no.8, 084054 [arXiv:1601.05588 [gr-qc]].
53. K. G. Arun, B. R. Iyer, B. S. Sathyaprakash and P. A. Sundararajan, Phys. Rev. D **71**, 084008 (2005) Erratum: [Phys. Rev. D **72**, 069903 (2005)] [gr-qc/0411146].
54. L. Blanchet, Living Rev. Rel. **17**, 2 (2014) [arXiv:1310.1528 [gr-qc]].
55. A. Bohé, S. Marsat and L. Blanchet, Class. Quant. Grav. **30**, 135009 (2013) [arXiv:1303.7412 [gr-qc]].
56. A. Bohé, G. Faye, S. Marsat and E. K. Porter, Class. Quant. Grav. **32**, 19, 195010 (2015) [arXiv:1501.01529 [gr-qc]].
57. S. Marsat, Class. Quant. Grav. **32**, 8, 085008 (2015) [arXiv:1411.4118 [gr-qc]].
58. K. Chatziioannou, E. Poisson and N. Yunes, Phys. Rev. D **94** (2016) no.8, 084043 [arXiv:1608.02899 [gr-qc]].
59. S. Isoyama and H. Nakano, Class. Quant. Grav. **35** (2018) no.2, 024001 [arXiv:1705.03869 [gr-qc]].
60. S. A. Hughes, Phys. Rev. D **100** (2019) no.6, 064001 [arXiv:1806.09022 [gr-qc]].
61. H. Nakano, H. Takahashi, H. Tagoshi and M. Sasaki, Phys. Rev. D **68**, 102003 (2003) [arXiv:gr-qc/0306082 [gr-qc]].
62. H. Nakano, H. Takahashi, H. Tagoshi and M. Sasaki, Prog. Theor. Phys. **111**, 781-805 (2004) [arXiv:gr-qc/0403069 [gr-qc]].
63. H. Nakano, T. Tanaka and T. Nakamura, Phys. Rev. D **92**, 064003 (2015) [arXiv:1506.00560 [astro-ph.HE]].
64. S. D. Mohanty, Phys. Rev. D **57**, 630-658 (1998) [arXiv:gr-qc/9703081 [gr-qc]].
65. J. Healy, C. O. Lousto and Y. Zlochower, Phys. Rev. D **90**, 104004 (2014) [arXiv:1406.7295 [gr-qc]].
66. F. Hofmann, E. Barausse and L. Rezzolla, Astrophys. J. Lett. **825** (2016) no.2, L19 [arXiv:1605.01938 [gr-qc]].
67. J. Healy and C. O. Lousto, Phys. Rev. D **95**, no.2, 024037 (2017) [arXiv:1610.09713 [gr-qc]].
68. X. Jiménez-Forteza, D. Keitel, S. Husa, M. Hannam, S. Khan and M. Pürrer, Phys. Rev. D **95** (2017) no.6, 064024 [arXiv:1611.00332 [gr-qc]].
69. J. Healy and C. O. Lousto, Phys. Rev. D **97**, no.8, 084002 (2018) [arXiv:1801.08162 [gr-qc]].
70. V. Varma, D. Gerosa, L. C. Stein, F. Hébert and H. Zhang, Phys. Rev. Lett. **122** (2019) no.1, 011101 [arXiv:1809.09125 [gr-qc]].
71. "Black Hole Perturbation Club (B.H.P.C.)", <https://sites.google.com/view/bhpc1996/home>.
72. E. Berti, V. Cardoso and A. O. Starinets, Class. Quant. Grav. **26**, 163001 (2009) [arXiv:0905.2975 [gr-qc]].
73. "Emanuele Berti's Ringdown", <https://pages.jh.edu/eberti2/ringdown/>.
74. G. B. Cook and M. Zaltowski, Phys. Rev. D **90**, 124021 (2014) [arXiv:1410.7698 [gr-qc]].
75. "Black Hole Perturbation Toolkit", <https://bhptoolkit.org/>.
76. E. Berti, V. Cardoso and C. M. Will, Phys. Rev. D **73**, 064030 (2006) [gr-qc/0512160].
77. P. Ajith, M. Hannam, S. Husa, Y. Chen, B. Bruegmann, N. Dorband, D. Muller, F. Ohme, D. Pollney and C. Reisswig, *et al.* Phys. Rev. Lett. **106**, 241101 (2011) [arXiv:0909.2867 [gr-qc]].
78. C. J. Moore, R. H. Cole and C. P. L. Berry, Class. Quant. Grav. **32** (2015) no.1, 015014 [arXiv:1408.0740 [gr-qc]].

79. L. S. Finn, *Phys. Rev. D* **46**, 5236 (1992) [gr-qc/9209010].
80. M. Vallisneri, *Phys. Rev. D* **77** (2008), 042001 [arXiv:gr-qc/0703086 [gr-qc]].
81. S. Babak, J. Gair, A. Sesana, E. Barausse, C. F. Sopuerta, C. P. L. Berry, E. Berti, P. Amaro-Seoane, A. Petiteau and A. Klein, *Phys. Rev. D* **95** (2017) no.10, 103012 [arXiv:1703.09722 [gr-qc]].
82. E. Poisson and C. M. Will, *Phys. Rev. D* **52** (1995), 848-855 [arXiv:gr-qc/9502040 [gr-qc]].
83. C. J. Moore, D. Gerosa and A. Klein, *Mon. Not. Roy. Astron. Soc.* **488** (2019) no.1, L94-L98 [arXiv:1905.11998 [astro-ph.HE]].
84. B. P. Abbott *et al.* [LIGO Scientific and Virgo], *Phys. Rev. Lett.* **116** (2016) no.22, 221101 [erratum: *Phys. Rev. Lett.* **121** (2018) no.12, 129902] [arXiv:1602.03841 [gr-qc]].
85. B. P. Abbott *et al.* [LIGO Scientific and Virgo], *Phys. Rev. D* **100** (2019) no.10, 104036 [arXiv:1903.04467 [gr-qc]].
86. Z. Carson and K. Yagi, *MDPI Proc.* **17**, no.1, 5 (2019) [arXiv:1908.07103 [gr-qc]].
87. R. Abbott *et al.* [LIGO Scientific and Virgo], [arXiv:2010.14529 [gr-qc]].
88. H. Nakano, T. Nakamura and T. Tanaka, *Prog. Theor. Exp. Phys.* (2016) 031E02 [arXiv:1602.02875 [gr-qc]].
89. F. Pretorius, *Phys. Rev. Lett.* **95**, 121101 (2005) [gr-qc/0507014].
90. M. Campanelli, C. O. Lousto, P. Marronetti, and Y. Zlochower, *Phys. Rev. Lett.* **96**, 111101 (2006) [gr-qc/0511048].
91. J. G. Baker, J. Centrella, D. I. Choi, M. Koppitz, and J. van Meter, *Phys. Rev. Lett.* **96**, 111102 (2006) [gr-qc/0511103].
92. K. Jani, J. Healy, J. A. Clark, L. London, P. Laguna and D. Shoemaker, *Class. Quant. Grav.* **33** (2016) no.20, 204001 [arXiv:1605.03204 [gr-qc]].
93. J. Healy, C. O. Lousto, Y. Zlochower and M. Campanelli, *Class. Quant. Grav.* **34** (2017) no.22, 224001 [arXiv:1703.03423 [gr-qc]].
94. J. Healy, C. O. Lousto, J. Lange, R. O'Shaughnessy, Y. Zlochower and M. Campanelli, *Phys. Rev. D* **100** (2019) no.2, 024021 [arXiv:1901.02553 [gr-qc]].
95. M. Boyle, D. Hemberger, D. A. B. Iozzo, G. Lovelace, S. Ossokine, H. P. Pfeiffer, M. A. Scheel, L. C. Stein, C. J. Woodford and A. B. Zimmerman, *et al.* *Class. Quant. Grav.* **36** (2019) no.19, 195006 [arXiv:1904.04831 [gr-qc]].
96. J. Healy and C. O. Lousto, *Phys. Rev. D* **102** (2020) no.10, 104018 [arXiv:2007.07910 [gr-qc]].
97. A. Ghosh, A. Ghosh, N. K. Johnson-McDaniel, C. K. Mishra, P. Ajith, W. Del Pozzo, D. A. Nichols, Y. Chen, A. B. Nielsen and C. P. L. Berry, *et al.* *Phys. Rev. D* **94** (2016) no.2, 021101 [arXiv:1602.02453 [gr-qc]].
98. A. Ghosh, N. K. Johnson-McDaniel, A. Ghosh, C. K. Mishra, P. Ajith, W. Del Pozzo, C. P. L. Berry, A. B. Nielsen and L. London, *Class. Quant. Grav.* **35** (2018) no.1, 014002 [arXiv:1704.06784 [gr-qc]].
99. S. A. Hughes and K. Menou, *Astrophys. J.* **623**, 689-699 (2005) [arXiv:astro-ph/0410148 [astro-ph]].
100. M. Luna and A. M. Sintes, *Class. Quant. Grav.* **23**, 3763-3782 (2006) [arXiv:gr-qc/0601072 [gr-qc]].
101. J. Veitch, V. Raymond, B. Farr, W. Farr, P. Graff, S. Vitale, B. Aylott, K. Blackburn, N. Christensen and M. Coughlin, *et al.* *Phys. Rev. D* **91**, no.4, 042003 (2015) [arXiv:1409.7215 [gr-qc]].
102. LIGO Scientific Collaboration, "LIGO Algorithm Library - LALSuite", <https://lscsoft.docs.ligo.org/lalsuite/lalsimulation/index.html> (2018) doi:10.7935/GT1W-FZ16
103. B. P. Abbott *et al.* [LIGO Scientific and Virgo], *Phys. Rev. Lett.* **116**, no.24, 241102 (2016) [arXiv:1602.03840 [gr-qc]].
104. T. D. Abbott *et al.* [LIGO Scientific and Virgo], *Phys. Rev. X* **6**, no.4, 041014 (2016) [arXiv:1606.01210 [gr-qc]].
105. H. Yang, K. Yagi, J. Blackman, L. Lehner, V. Paschalidis, F. Pretorius and N. Yunes, *Phys. Rev. Lett.* **118**, no.16, 161101 (2017) [arXiv:1701.05808 [gr-qc]].
106. K. D. Kokkotas and B. G. Schmidt, *Living Rev. Rel.* **2**, 2 (1999) [arXiv:gr-qc/9909058 [gr-qc]].
107. H. P. Nollert, *Class. Quant. Grav.* **16**, R159-R216 (1999).
108. R. P. Kerr, *Phys. Rev. Lett.* **11**, 237 (1963).
109. M. Sasaki and T. Nakamura, *Phys. Lett. A* **89**, 68 (1982).
110. M. Sasaki and T. Nakamura, *Prog. Theor. Phys.* **67**, 1788 (1982).
111. T. Nakamura and M. Sasaki, *Phys. Lett. A* **89**, 185 (1982).
112. S. A. Teukolsky, *Astrophys. J.* **185**, 635 (1973).
113. T. Nakamura and H. Nakano, *Prog. Theor. Exp. Phys.* (2016) 041E01 [arXiv:1602.02385 [gr-qc]].
114. T. Nakamura, K. Oohara and Y. Kojima, Part III of *Prog. Theor. Phys. Suppl.* **90** (1987), 1-218

115. R. A. Konoplya and A. Zhidenko, *Rev. Mod. Phys.* **83**, 793-836 (2011) [arXiv:1102.4014 [gr-qc]].
116. E. W. Leaver, *Proc. Roy. Soc. Lond. A* **402**, 285 (1985).
117. B. F. Schutz and C. M. Will, *Astrophys. J. Lett.* **291**, L33-L36 (1985)
118. S. Iyer and C. M. Will, *Phys. Rev. D* **35**, 3621 (1987)
119. R. A. Konoplya, *Phys. Rev. D* **68**, 024018 (2003) [arXiv:gr-qc/0303052 [gr-qc]].
120. R. A. Konoplya, *J. Phys. Stud.* **8**, 93-100 (2004)
121. J. Matyjasek and M. Opala, *Phys. Rev. D* **96**, no.2, 024011 (2017) [arXiv:1704.00361 [gr-qc]].
122. R. A. Konoplya, A. Zhidenko and A. F. Zinhailo, *Class. Quant. Grav.* **36**, 155002 (2019) [arXiv:1904.10333 [gr-qc]].
123. H. Nakano, N. Sago, T. Tanaka and T. Nakamura, *PTEP* **2016**, no.8, 083E01 (2016) [arXiv:1604.08285 [gr-qc]].
124. G. Khanna and R. H. Price, *Phys. Rev. D* **95**, no.8, 081501 (2017) [arXiv:1609.00083 [gr-qc]].
125. R. A. Konoplya and Z. Stuchlík, *Phys. Lett. B* **771**, 597-602 (2017) [arXiv:1705.05928 [gr-qc]].
126. K. Glampedakis, G. Pappas, H. O. Silva and E. Berti, *Phys. Rev. D* **96**, no.6, 064054 (2017) [arXiv:1706.07658 [gr-qc]].
127. T. Regge and J. A. Wheeler, *Phys. Rev.* **108**, 1063 (1957).
128. F. J. Zerilli, *Phys. Rev. D* **2**, 2141-2160 (1970)
129. S. Chandrasekhar, *The mathematical theory of black holes*, OXFORD, UK: CLARENDON (1985).
130. H. Yang, D. A. Nichols, F. Zhang, A. Zimmerman, Z. Zhang and Y. Chen, *Phys. Rev. D* **86**, 104006 (2012) [arXiv:1207.4253 [gr-qc]].
131. N. Sago and T. Tanaka, [arXiv:2009.08086 [gr-qc]].
132. T. Nakamura, H. Nakano and T. Tanaka, *Phys. Rev. D* **93**, 044048 (2016) [arXiv:1601.00356 [astro-ph.HE]].
133. J. M. Bardeen, W. H. Press and S. A. Teukolsky, *Astrophys. J.* **178**, 347 (1972)
134. S. L. Detweiler, *Proc. Roy. Soc. Lond. A* **352**, 381 (1977).
135. S. Isoyama, R. Sturani and H. Nakano, [arXiv:2012.01350 [gr-qc]].
136. C. M. Biwer, C. D. Capano, S. De, M. Cabero, D. A. Brown, A. H. Nitz and V. Raymond, *Publ. Astron. Soc. Pac.* **131** (2019) no.996, 024503 [arXiv:1807.10312 [astro-ph.IM]].
137. G. Ashton, M. Hübner, P. D. Lasky, C. Talbot, K. Ackley, S. Biscoveanu, Q. Chu, A. Divakarla, P. J. Easter and B. Goncharov, *et al.* *Astrophys. J. Suppl.* **241** (2019) no.2, 27 [arXiv:1811.02042 [astro-ph.IM]].
138. B. Ireland, O. Birnholtz, H. Nakano, E. West and M. Campanelli, *Phys. Rev. D* **100**, no.2, 024015 (2019) [arXiv:1904.03443 [gr-qc]].
139. R. Abbott *et al.* [LIGO Scientific and Virgo], *Astrophys. J. Lett.* **896**, no.2, L44 (2020) [arXiv:2006.12611 [astro-ph.HE]].
140. L. London, S. Khan, E. Fauchon-Jones, C. García, M. Hannam, S. Husa, X. Jiménez-Forteza, C. Kalaghatgi, F. Ohme and F. Pannarale, *Phys. Rev. Lett.* **120**, no.16, 161102 (2018) [arXiv:1708.00404 [gr-qc]].
141. K. Sakai, K. I. Oohara, H. Nakano, M. Kaneyama and H. Takahashi, *Phys. Rev. D* **96**, no.4, 044047 (2017) [arXiv:1705.04107 [gr-qc]].
142. G. Carullo, L. Van Der Schaaf, L. London, P. T. H. Pang, K. W. Tsang, O. A. Hannuksela, J. Meidam, M. Agathos, A. Samajdar and A. Ghosh, *et al.* *Phys. Rev. D* **98**, no.10, 104020 (2018) [arXiv:1805.04760 [gr-qc]].
143. M. Giesler, M. Isi, M. A. Scheel and S. Teukolsky, *Phys. Rev. X* **9**, no.4, 041060 (2019) [arXiv:1903.08284 [gr-qc]].
144. M. Isi, M. Giesler, W. M. Farr, M. A. Scheel and S. A. Teukolsky, *Phys. Rev. Lett.* **123**, no.11, 111102 (2019) [arXiv:1905.00869 [gr-qc]].
145. S. Bhagwat, X. J. Forteza, P. Pani and V. Ferrari, *Phys. Rev. D* **101**, no.4, 044033 (2020) [arXiv:1910.08708 [gr-qc]].
146. I. Ota and C. Chirenti, *Phys. Rev. D* **101**, no.10, 104005 (2020) [arXiv:1911.00440 [gr-qc]].
147. H. Nakano, T. Narikawa, K. i. Oohara, K. Sakai, H. a. Shinkai, H. Takahashi, T. Tanaka, N. Uchikata, S. Yamamoto and T. S. Yamamoto, *Phys. Rev. D* **99**, no.12, 124032 (2019) [arXiv:1811.06443 [gr-qc]].
148. T. S. Yamamoto and T. Tanaka, [arXiv:2002.12095 [gr-qc]].
149. Z. Carson and K. Yagi, [arXiv:2011.02938 [gr-qc]].
150. S. L. Detweiler, *Astrophys. J.* **239**, 292-295 (1980)
151. O. Dreyer, B. J. Kelly, B. Krishnan, L. S. Finn, D. Garrison and R. Lopez-Aleman, *Class. Quant. Grav.* **21**, 787-804 (2004) [arXiv:gr-qc/0309007 [gr-qc]].

152. E. Berti, A. Sesana, E. Barausse, V. Cardoso and K. Belczynski, *Phys. Rev. Lett.* **117**, no.10, 101102 (2016) [arXiv:1605.09286 [gr-qc]].
153. V. Baibhav and E. Berti, *Phys. Rev. D* **99**, no.2, 024005 (2019) [arXiv:1809.03500 [gr-qc]].
154. G. Gnocchi, A. Maselli, T. Abdelsalhin, N. Giacobbo and M. Mapelli, *Phys. Rev. D* **100** (2019) no.6, 064024 [arXiv:1905.13460 [gr-qc]].
155. E. Berti, J. Cardoso, V. Cardoso and M. Cavaglia, *Phys. Rev. D* **76**, 104044 (2007) [arXiv:0707.1202 [gr-qc]].
156. T. Akutsu *et al.* [KAGRA], [arXiv:2008.02921 [gr-qc]].
157. N. Uchikata, T. Narikawa, K. Sakai, H. Takahashi and H. Nakano, *Phys. Rev. D* **102**, no.2, 024007 (2020) [arXiv:2003.06791 [gr-qc]].
158. R. Tso, D. Gerosa and Y. Chen, *Phys. Rev. D* **99** (2019) no.12, 124043 [arXiv:1807.00075 [gr-qc]].
159. C. O. Lousto, private communication (2020).
160. I. M. Romero-Shaw, P. D. Lasky, E. Thrane and J. C. Bustillo, *Astrophys. J. Lett.* **903** (2020) no.1, L5 [arXiv:2009.04771 [astro-ph.HE]].
161. J. Calderón Bustillo, N. Sanchis-Gual, A. Torres-Forné and J. A. Font, [arXiv:2009.01066 [gr-qc]].
162. P. C. Peters and J. Mathews, *Phys. Rev.* **131**, 435-439 (1963).
163. P. C. Peters, *Phys. Rev.* **136**, B1224-B1232 (1964).
164. M. Maggiore, *Gravitational Waves. Vol. 1: Theory and Experiments*, Oxford University Press, Oxford, England (2014).
165. P. Amaro-Seoane, *Phys. Rev. D* **98**, no.6, 063018 (2018) [arXiv:1807.03824 [astro-ph.HE]].
166. A. M. Holgado, A. Ortega and C. L. Rodriguez, [arXiv:2012.09169 [astro-ph.HE]].
167. P. Amaro-Seoane, M. C. Miller and M. Freitag, *Astrophys. J. Lett.* **692** (2009), L50-L53 [arXiv:0901.0604 [astro-ph.SR]].
168. N. Loutrel, [arXiv:2009.11332 [gr-qc]].
169. L. S. Finn and K. S. Thorne, *Phys. Rev. D* **62** (2000), 124021 [arXiv:gr-qc/0007074 [gr-qc]].
170. E. A. Huerta, S. T. McWilliams, J. R. Gair and S. R. Taylor, *Phys. Rev. D* **92** (2015) no.6, 063010 [arXiv:1504.00928 [gr-qc]].
171. C. Cutler, D. Kennefick and E. Poisson, *Phys. Rev. D* **50** (1994), 3816-3835
172. L. Gondán, B. Kocsis, P. Raffai and Z. Frei, *Astrophys. J.* **855** (2018) no.1, 34 [arXiv:1705.10781 [astro-ph.HE]].
173. B. Mikoczi, B. Kocsis, P. Forgacs and M. Vasuth, *Phys. Rev. D* **86** (2012), 104027 [arXiv:1206.5786 [gr-qc]].
174. S. Drasco and S. A. Hughes, *Phys. Rev. D* **73** (2006) no.2, 024027 [erratum: *Phys. Rev. D* **88** (2013) no.10, 109905; erratum: *Phys. Rev. D* **90** (2014) no.10, 109905] [arXiv:gr-qc/0509101 [gr-qc]].
175. A. Nishizawa, E. Berti, A. Klein and A. Sesana, *Phys. Rev. D* **94** (2016) no.6, 064020 [arXiv:1605.01341 [gr-qc]].
176. N. Seto, *Mon. Not. Roy. Astron. Soc.* **460** (2016) no.1, L1-L4 [arXiv:1602.04715 [astro-ph.HE]].
177. R. Abbott *et al.* [LIGO Scientific and Virgo], [arXiv:2010.14533 [astro-ph.HE]].
178. T. Kinugawa, T. Nakamura and H. Nakano, [arXiv:2007.13343 [astro-ph.HE]].
179. B. P. Abbott *et al.* [KAGRA, LIGO Scientific and VIRGO], *Living Rev. Rel.* **23**, 3 (2020) [arXiv:1304.0670 [gr-qc]].
180. S. Hild, S. Chelkowski and A. Freise, [arXiv:0810.0604 [gr-qc]].
181. C. K. Mishra, K. G. Arun, B. R. Iyer and B. S. Sathyaprakash, *Phys. Rev. D* **82**, 064010 (2010) [arXiv:1005.0304 [gr-qc]].
182. "ET sensitivities page", <http://www.et-gw.eu/index.php/etsensitivities>.
183. K. Yagi and N. Seto, *Phys. Rev. D* **83** (2011), 044011 [erratum: *Phys. Rev. D* **95** (2017) no.10, 109901] [arXiv:1101.3940 [astro-ph.CO]].
184. X. C. Hu, X. H. Li, Y. Wang, W. F. Feng, M. Y. Zhou, Y. M. Hu, S. C. Hu, J. W. Mei and C. G. Shao, *Class. Quant. Grav.* **35** (2018) no.9, 095008 [arXiv:1803.03368 [gr-qc]].
185. C. Shi, J. Bao, H. Wang, J. d. Zhang, Y. Hu, A. Sesana, E. Barausse, J. Mei and J. Luo, *Phys. Rev. D* **100** (2019) no.4, 044036 [arXiv:1902.08922 [gr-qc]].